



Derived-2D Nb₄C₃T_x sheets with interfacial self-assembled Fe-N-C single-atom catalyst for electrocatalysis in water splitting and durable zinc-air battery

Mahmood ul Haq, Dong-Hui Wu, Zeeshan Ajmal, Qi-Dong Ruan, Shahid Khan, Lu Zhang, Ai-Jun Wang^{*}, Jiu-Ju Feng^{*}

Key Laboratory of the Ministry of Education for Advanced Catalysis Materials, College of Chemistry and Materials Science, College of Geography and Environmental Sciences, Zhejiang Normal University, Jinhua 321004, China

ARTICLE INFO

Keywords:

Nb₄C₃T_x-MXene
Fe-N-C
Theory calculations
Water splitting
Zinc-air battery

ABSTRACT

In pursuit of advanced nanocatalysts with multifunctionality, cost-effectiveness and durability for water splitting and zinc-air batteries, we unveil a novel strategy by combination of electrochemically etched Nb₄C₃T_x-MXene nanosheets with Fe-N-C single-atom catalyst. The resultant Fe-N-C/Nb₄C₃T_x demonstrates exceptional electrocatalytic performances for the ORR ($E_{1/2} = 0.911$ V), OER ($\eta_{10} = 1.52$ V), and HER ($\eta_{10} = 91$ mV) in the alkaline media. Besides, the catalyst shows excellent application in water splitting electrolyzer, only requiring 1.58 V for a current density of 10 mA cm⁻². Further, the Fe-N-C/Nb₄C₃T_x assembled battery displays an open-circuit voltage of 1.51 V, a higher peak power density (136 mW cm⁻²), a narrower polarization gap (0.85 V), and remarkable stability (660 cycles over 220 h), surpassing the Pt/C + RuO₂ based counterpart. Our study integrates DFT calculations to guide the catalyst design, laying the foundation for development of reliable and effective tri-functional catalysts in advanced energy-related systems.

1. Introduction

Green energy innovations (e.g., water electrolysis, hydrogen fuel, and energy storage systems) have garnered substantial attention in the context of increasing air pollution and the world's energy conflict [1–4]. Generally, oxygen reduction reaction (ORR) is imperative in rechargeable liquid batteries and fuel cells [4]. In contrast, hydrogen evolution reaction (HER) and oxygen evolution reaction (OER) are two prominent half-reactions observed in water electrolysis [4,5]. Zinc-air batteries are considered favorable configurations for their high theoretical charging capacity and abundant zinc source [1,6].

Currently, the leading edge of zinc-air batteries lies in physico-chemical structure design of the air cathode, which involves diverse bifunctional electrocatalysts [7]. Without a proper material design, the intermediated oxygen reactions are commonly slow, leading to a low power generation [8]. Usually, Pt- or RuO₂/IrO₂-based catalysts are recognized as gold standard for the ORR, OER, and HER, albeit with their high price [9,10]. However, their limited tolerance and instability have severely hampered the practical commercialization [4,11]. To

overcome these obstacles, it is very urgent to fabricate novel electrocatalyst that simultaneously promotes the above reactions [5,12].

Metal-organic frameworks (MOFs) are currently recognized as starting materials for production of metallic single-atom catalyst with nitrogen-doped carbon (M-N-C SAC), owing to their large surface areas, numerous active sites, and homogeneous modification of heteroatoms [13–15]. Moreover, MOFs with different metal ions can effectively adjust the intrinsic electronic and surface structures of the derivatives, and bestow the resulting products with hollow and porous structures, ultimately improving the electrocatalytic performances [16,17]. Regrettably, these derivatives are susceptible aggregated together during the electrocatalysis course, and thus reduce the active surface area, in turn deteriorating the catalytic activity. Therefore, it is urgent for synthesis of advanced MOFs derivatives with superior catalytic performance.

To address this issue, carbonaceous materials [18] such as carbon-nanotubes [19], and two-dimensional (2D) graphene [20,21] were employed, showing the significantly improved ORR activity and stability. For example, Fe-doped ZIF-67 was annealed to prepare

^{*} Corresponding authors.

E-mail addresses: ajwang@zjnu.cn (A.-J. Wang), jjfeng@zjnu.cn (J.-J. Feng).

<https://doi.org/10.1016/j.apcatb.2023.123632>

Received 6 July 2023; Received in revised form 22 November 2023; Accepted 3 December 2023

Available online 18 December 2023

0926-3373/© 2023 Elsevier B.V. All rights reserved.

nitrogen-treated graphene with mesoporous structure, which exhibited the better ORR performance with high current densities and positive half-wave potential ($E_{1/2} = 0.84$ V) [22]. In another example, a series of benzene-tricarboxylate (BTC) catalysts were prepared by modifying the configuration of the MOFs precursor, which showed comparable ORR and HER performances to commercial Pt/C and IrO₂ catalysts [23]. However, carbon matrix have widely employed in most of the previous research, while less work was done on the highly conductive non-carbon supports.

Since Yury presented 2D transition-metal carbide (termed MXene) in 2011, whose family has been the focus of much interest in in-depth research over the last ten years [24,25]. Apart from the substantial surface area and efficient electric conductivity, the versatility of surface functional groups on MXenes allows them to have varying catalytic efficacy. Therefore, MXenes had received much attention in energy renovation, including lithium-sulfur batteries [26], Li-O₂ batteries [27], and Zn-air batteries [2,28].

Recent studies reveal that transition metal like niobium in Nb₂CT_x (T = F, O, OH, etc.) has a greater metallicity and more unsaturated valence electrons than well-researched Ti₃C₂T_x [29]. On the one hand, Nb₂CT_x has superior electric conductivity over Ti₃C₂T_x. Consequently, Nb₂CT_x absorbs more oxygen rapidly to produce oxygen-containing functional groups, which benefits the ORR and OER activities [27]. However, their some drawbacks (e.g., easy aggregation, self-accumulation, and poor thermal stability) result in slow reaction kinetics [3]. To address these issues, MXene-supported MOFs derivatives were utilized to bolster thermal stability, shield against high temperature, and enhance catalytic activity in water electrolysis [30,31]. The MOFs structure can effectively act as a heat sink, and dissipate heat away from the MXene, ultimately improving overall thermal performance. It's imperative to carefully select the appropriate MOFs derivatives, as the composite may exhibit synergistic interactions between MXene and M-N-C catalysts, which hold the potential to improve charge/mass transport, mitigate catalyst aggregation, and further enhance thermal performance [30].

Herein, a self-assembly technique was adopted to embed the Fe-N-C SAC into oxygen-terminated Nb₄C₃T_x-MXene for the first time. The tri-functional electrocatalytic performances (i.e., ORR, OER, and HER) of the optimized Fe-N-C/Nb₄C₃T_x were scrutinized in the alkaline electrolytes, exploring its potential applications in water electrolysis and Zn-air batteries. Moreover, the Fe-N-C/Nb₄C₃T_x-based Zn-air battery was assessed, coupled by checking the open-circuit potential, peak power density, and prolonged stability.

2. Experimental

2.1. Chemicals

Briefly, the follow-up chemicals were all standard grade, including MAX (Nb₄AlC₃), zinc nitrate hexahydrate (Zn(NO₃)₂•6 H₂O), tris(acetylacetonato) iron(III) (Fe(C₅H₇O₂)₃), commercial Pt/C (50 wt.%), RuO₂, 2-methylimidazole, potassium hydroxide (KOH), zinc acetate (Zn(CH₃COOH)₂), N, N-dimethylformamide (DMF), methanol (CH₃OH), hydrochloric acid (HCl), dimethyl sulfoxide (DMSO), carbon black (CB), and carbon fiber cloth (CFC). All of them were received from Aladdin Chemical Reagent Cooperation (Shanghai) and used without any additional treatment.

2.2. Synthesis of the Nb₄C₃T_x

First, Nb₄AlC₃ (MAX > 99%, Beijing Beike New Material Technology Co., Ltd) and carbon black (CB) were mixed at a weight ratio of 95: 5, where 1.00 mL of a polyvinyl alcohol aqueous solution (1 wt.%) acted as a binder. To ensure precisely mixing, 10 mg of the mixture was crushed and ultra-sonicated for 30 min, and then the paste was cast on carbon fiber cloth (CFC, 1 cm × 2 cm) [32]. Next, the modified electrode was

electrochemically etched (E-etching) in a diluted HCl solution (1.0 M) by applying a series of potentials (e.g., 0.3, 0.6, and 1.0 V) for 3 h at 25 and 50 °C, respectively.

After such treatment, the freshly etched MXene was extracted from the CFC by thoroughly washing with ethanol under ultrasonication for 60 s, followed by centrifuging and completely washing with water to harvest layered Nb₄C₃T_x sheets (where T_x refers to O or OH). The as-collected Nb₄C₃T_x was subsequently immersed into DMSO, ultra-sonicated for 3 h, rinsed with water to eradicate the unetched Al phase and CB, and vacuum-dried overnight at 60 °C, ultimately harvesting the Nb₄C₃T_x.

2.3. Synthesis of the Fe-N-C

The Fe-doped ZIF-8 was initially prepared according to the earlier research [15]. In short, 1.5 g of Zn(NO₃)₂•6 H₂O and 0.22 g of Fe(Acac)₃ were put into 20 mL of methanol (solution A). In parallel, 3.25 g of 2-methylimidazole was placed into 40 mL of methanol (solution B). The solution A was then dropped into the solution B and magnetically stirred for 24 h at ambient temperature. The reaction mixture was centrifuged, rinsed with methanol, and then vacuum-dried at 60 °C overnight, harvesting the Fe-doped ZIF-8. For pyrolysis synthesis of the Fe-N-C in the control groups, the Fe-doped ZIF-8 was subjected to a temperature ramp with a rate of 5 °C min⁻¹ and remained at a series of temperature (e.g., 600, 850, and 1000 °C) in nitrogen atmosphere for 2 h, achieving the release of volatile Zn ions.

2.4. Synthesis of the Fe-N-C/MXene

The Fe-N-C catalysts were evenly deposited onto the Nb₄C₃T_x sheets by dispersing them into DMF at various weight ratios (e.g., 1:1, 2:1, 1:2, 3:1, 4:1, and 6:1) under ultrasonication for 4 h. The gathered samples were centrifuged, washed with DMF and methanol, and vacuum-dried overnight at 60 °C. The final hybrid product was then pyrolyzed in a range of the temperature (e.g., 100, 200, 250, and 300 °C) under N₂-saturated conditions for 2 h at a heating rate of 5 °C min⁻¹, eventually accomplishing the assembly of Fe-N-C catalysts onto the Nb₄C₃T_x sheets (termed Fe-N-C/MXene for clarity).

2.5. Characterizations

The structure texture and elemental configurations of the catalysts were perceived through scanning electron microscope (SEM with a model Hitachi S-400) at a working potential of 15 kV, transmission electron microscope (TEM with a model JEM-2100 F), coupled with element mapping analyzer (STEM) at an operating potential of 200 kV. The crystal features were obtained through X-ray diffractometer (XRD with a model PW3040/60) operated at an excitation wavelength of 0.15405 nm, coupled with Cu Kα as X-ray source. The surface defects and graphitization were scrutinized through Raman spectrometer (Renishaw-100 model) operated with an excitation wavelength of 532 nm laser source. The superficial porosity measurements were performed through BET analyzer (Beishide-3 H-2000PS2) by acquiring the N₂ adsorption/desorption isotherms. The catalyst's oxidation states were assessed by X-ray photoelectron spectroscopy where an Al Kα acted as X-ray source at a Thermo-VG ESCALAB-250 spectrometer.

The X-ray absorption fine structure (XAFS) spectra were acquired at the 1W1B station within the Beijing Synchrotron Radiation Facility (BSRF), utilizing the synchrotron's storage ring operating at 2.5 GeV. The storage ring consistently generated the maximum current beam of 250 mA during the experiments. To capture the absorption spectra of the Fe K-edge, the fluorescence excitation mode was employed by utilizing a Si (111) double-crystal monochromator at room temperature, coupled with a Lytle detector. For comparative analysis, Fe foil and Fe₂O₃ samples were employed and measured by using an ionization chamber in transmission mode.

Subsequently, the EXAFS data underwent a series of processes including analysis, reduction, and fitting, facilitated by the Athena-Artemis software programs within the Demeter data analysis suite. Notably, the suite incorporates the FEFF6 program specifically designed for EXAFS data fitting. To ensure precise energy calibration, a typical Fe foil was employed as a reference and concurrently assessed. In the preprocessing steps, a linear function was deducted from the pre-edge section, and the normalization of the edge shift was executed using the Athena software. The isolation of $\chi(k)$ data entailed subtracting a sophisticated three-staged polynomial approximation representing the absorption background associated to an isolated atom, thereby ensuring the accuracy of the analysis.

To prepare the data for EXAFS modeling, a Kaiser-Bessel window function ($\Delta k = 1.0$) was applied, and Fourier transformation of the k^2 -weighted $\chi(k)$ data were performed. The global amplitude EXAFS parameters (e.g., CN, R, σ^2 and ΔE_0) for the modeling process were determined through a nonlinear fitting procedure by utilizing least-squares refinement. This fitting process was executed by using the Artemis software. Notably, the EXAFS of the Fe foil was employed as a reference, and the amplitude reduction factor S_0^2 value (0.70, obtained from this reference) was applied in the EXAFS analysis to ascertain the coordination numbers (CNs) related to the Fe-O/N scattering track within the material.

2.6. Electrochemical experiments

The electrochemical assessments were explored on a CHI-660E workstation (purchased from Chenhua Instrument Cooperation, Shanghai). A standard 3-electrode setup was used to supervise the ORR courses, with a catalyst-loaded glassy carbon rotating disk electrode (RDE, $\Phi = 3$ mm), a carbon rod and a saturated-calomel electrode (SCE) as working, counter and reference electrodes, respectively. The electrochemical potentials referenced against the SCE were converted to those of a typical reversible hydrogen electrode (RHE) according to the following transformation formula [2,4]:

$$E_{\text{RHE}} = E_{\text{SCE}} + 0.059 \text{ pH} + 0.241 \quad (1)$$

For standard preparation of the catalyst ink, 5 mg of the as-prepared sample was evenly dispersed into a blend of ethanol (0.50 mL), water (0.47 mL), and a 5 wt.% Nafion solution (30 μL) under ultrasonication for 30 min. Subsequently, 16 μL of the resulting suspension was cast onto a freshly cleaned RDE with a mass loading of 0.35 mg cm^{-2} . Similarly, a standard Pt/C-coated electrode was also fabricated in the control groups with a mass loading of 0.15 mg cm^{-2} .

Cyclic voltammetry curves for the synthesized electrocatalyst were acquired in both O_2 - and N_2 -saturated 0.1 M KOH electrolyte at a scan rate of 50 mV s^{-1} . Simultaneously, linear sweep voltammetry (LSV) curves were recorded under O_2 -saturated conditions at a sweep rate of 5 mV s^{-1} . The electrochemical impedance spectroscopy (EIS) test was implemented, and the corresponding Nyquist plots were recorded. The electrochemical active surface area (ECSA) was meticulously evaluated by CV in the O_2 -saturated alkaline solution at a series of scan rates (i.e., 2, 4, 6, 8, and 10 mV s^{-1}). The double-layer capacitance (C_{dl}) refers to the slope of the linear segment in the graph, and the ECSA was calculated through the following formula [2,5]:

$$\text{ECSA} = C_{\text{dl}}/C_s \quad (2)$$

where C_s is the specific capacitance with a value of 0.04 mF cm^{-2} .

The hydrogen peroxide yield (%) and number of electron transfer (n) on the rotating ring-disk electrode (RRDE) can be derived from the follow-up equations [5,28]:

$$\text{H}_2\text{O}_2 (\%) = 200 \times \frac{\frac{I_{\text{Ring}}}{N}}{\left(\frac{I_{\text{Ring}}}{N}\right) + I_{\text{Disk}}} \quad (3)$$

$$n = 4 \times \frac{I_{\text{Disk}}}{\left(\frac{I_{\text{Ring}}}{N}\right) + I_{\text{Disk}}} \quad (4)$$

where N is the collection efficiency (37%), I_{Disk} and I_{Ring} represent the electrochemical currents on the disk- and ring-electrode, respectively.

The LSV curves for the OER and HER were recorded in a 1.0 M alkaline solution at 5 mV s^{-1} . The catalyst-modified Ni foam ($1.2 \times 0.5 \text{ cm}^2$) worked as the working electrode with a catalyst loading of 1.0 mg cm^{-2} , while the other conditions accorded well with those of the ORR if not specifically stated. For the comparative study, commercial Pt/C, RuO_2 , and bare Ni-foam were behaved as the control catalysts in this research. In addition, the stability and durability tests were investigated by chronopotentiometry. The electrochemical measurements were repeated for at least three times ($n = 3$) to ensure consistent experimental findings.

2.7. Overall water splitting test

To assess the overall efficacy of water splitting, a conventional two-electrode configuration was implemented within a 1.0 M KOH solution. The as-prepared catalysts were deposited onto the Ni foams, and utilized as the anode and cathode. The catalysts were loaded at a mass density of 1.0 mg cm^{-2} . The LSV plots were recorded at 5 mV s^{-1} .

2.8. DFT calculations

The Vienna ab initio simulation software utilized the projector augmented plane-wave (PAW) technique was implemented for all DFT calculations [33]. The initial optimization of the Fe-N-C/ $\text{Nb}_4\text{C}_3\text{T}_x$ structure was conducted by using the VASP package. Both $\text{Nb}_4\text{C}_3\text{T}_x$ and Fe-N-C exhibit hexagonal crystalline structures. To perform these calculations, a Monkhorst-Pack grid was employed with a $2 \times 2 \times 1$ mesh for the k-point selection of the Fe-N-C/ $\text{Nb}_4\text{C}_3\text{T}_x$ heterostructure, where isolated Fe-N-C and $\text{Nb}_4\text{C}_3\text{T}_x$ behaved as the references.

The exchange-correlation potential was determined by employing the normalized gradient approach recommended by Perdew-Burke-Ernzerhof (PBE) [34]. To solve the Kohn-Sham equation iteratively, a threshold energy of 480 eV for plane waves was implemented, in conjunction with an energy constraint of 10^{-5} eV. The structural optimization continued until the atomic residual forces fell below 0.02 eV/Å. Additionally, a perpendicular vacuum spacing of 20 Å was applied to the slab to mitigate the interlaminar interactions.

To provide a basis for comparison, the density of states (DOS) was computed individually for Fe-N-C, $\text{Nb}_4\text{C}_3\text{T}_x$, and Fe-N-C/ $\text{Nb}_4\text{C}_3\text{T}_x$. Moreover, the Gibbs' free energy and the molecules' adsorption energy were assessed by using VASPKIT. The calculation of adsorption energy can be determined by employing the following formula:

$$E_a = E_{\text{total}} - (E_{\text{O}_2} + E_*) \quad (5)$$

where E_{total} , E_{O_2} , and E_* are the energies of O_2 adsorbing substrate, O_2 , and Fe-N-C/ $\text{Nb}_4\text{C}_3\text{T}_x$, respectively.

2.9. Zn-air battery test

A home-made battery was devised, featuring a newly refined Zn plate as the air-anode, a carbon paper coated with the prepared catalyst as the air-cathode at a loading of 1.0 mg cm^{-2} , and an electrolyte blend comprising 6.0 M KOH and 0.2 M zinc acetate. The LSV curves were recorded to investigate the power-density and prolonged cycling stability. The operating interval for a single charge/discharge cycle was 20 min. A Pt/C + RuO_2 based battery was constructed by the same way in the control group for the comparative analysis.

3. Results and discussion

3.1. Characterizations

Fig. 1 reveals the schematic diagram of the fabrication procedure for the Fe-N-C/Nb₄C₃T_x. First, the Nb₄C₃T_x was designated for validating the developed electrochemical etching treatment of Nb₄AlC₃ with chlorine etchant to stimulate the more efficient electrochemical operation [35]. The Nb₄AlC₃-CB/CFC shows the higher redox peak currents at 0.43 V and 0.48 V when compared with those of the Nb₄AlC₃/CFC in the control tests (Fig. S1a), and the 3D-composite electrode exhibits a lower charge transfer resistance ($R_{ct} = 2465 \Omega$) in the acidic solution (Fig. S1b), thereby indicating its significant contribution in lowering the resistance [36]. An ideal voltage was chosen as the etching potential to encourage the more selective elimination of Al ions and prevent over-etching (Fig. S1c), because the Nb-Al bond is weaker than the Nb-C bond [37,38]. Moreover, the mild heating stimulates the Nb₄AlC₃ etching by increasing the current intensity of the E-etch system as the temperature ascends from 25 to 50 °C (Fig. S1c).

In order to increase the surface utilization, several-layered Nb₄C₃T_x sheets were harvested by an ultrasonic separation of multilayered Nb₄C₃T_x in DMSO. Secondly, the layered Nb₄C₃T_x worked as support to incorporate the Fe-N-C catalysts by ultrasonication in DMF, followed by pyrolyzing at a series of temperature, finally harvesting the optimal electrocatalyst (i.e., Fe-N-C/Nb₄C₃T_x).

The structural texture of the as-obtained samples was studied by SEM and TEM characterizations. In stark contrast to the flat surface of unetched Nb₄AlC₃ (Fig. S2a), low voltage (0.3 V) with mild heating causes delamination and a coarser texture for Nb₄C₃T_x (Fig. S2b), while over-etching (Fig. S2c) occurs at a higher voltage (1.0 V). Fig. 2a shows the morphology of the layered Nb₄C₃T_x sheets via E-etching at 0.6 V, which exhibits an accordion-like structure. The wavy flakes of MXene with layer spacing are resilient for the intense coupling of Fe-N-C catalysts. Such a structural renovation indicates successful E-etching, particularly in thermal exposure.

As depicted by the SEM image, there typically show 2–3 layers for the Nb₄C₃T_x (Fig. 2b) with an average layer thickness of 20–30 nm. Fig. 2c–d illustrates the morphological characteristics of the as-synthesized Fe-N-C catalyst (carbonized at 850 °C). As the SEM and TEM images

exhibit, the carbonized Fe-N-C has a distinctive dodecahedron shape with an average particle size of 80–100 nm. Further, single Fe atoms are observed as distinct isolated bright dots based on the aberration-corrected atomic-resolution high-angle annular dark-field scanning transmission electron microscopy (HAADF-STEM) analysis (Fig. 2e). Impressively, there exhibit a large number of independent bright spots, which demonstrate that the single Fe atoms display uniform distributions within the carbon frameworks. The homogenous distributions of Fe, N, and C elements throughout the entire carbon skeleton were confirmed by the HAADF-STEM and EDS mapping analysis (Fig. S3, SI).

Furthermore, the high temperature conducts somewhat altered the configuration of the Fe-N-C, and the nanoparticle size was reduced to some extent, thereby aggregation and collapsing occur during the combustion process, which would be detrimental to the mass/charge transport. Fig. 2f–g displays the morphological structure of the Fe-N-C/Nb₄C₃T_x (2:1) sample after the pyrolysis at 200 °C. The SEM images at low- and high-magnification unveil that the Fe-N-C nanoparticles are firmly and well-distributed on the interface and surface of the Nb₄C₃T_x sheet, where the aggregation of the Fe-N-C nanoparticles is markedly reduced.

As the TEM image (Fig. 2h) reflects, the Fe-N-C nanoparticles are uniformly distributed across the layered surface of the Nb₄C₃T_x substrate. The well-defined lattice fringes emerge in the high-resolution TEM image of the Fe-N-C/Nb₄C₃T_x (2:1, Fig. 2i). The relevant lattice spacing distance of 0.595 nm well aligns to the (004) crystal planes of the Nb₄C₃T_x-MXene [39].

Fig. S2d–f displays the SEM images of the Fe-N-C/Nb₄C₃T_x (1:1) and Fe-N-C/Nb₄C₃T_x (4:1), Fe-N-C/Nb₄C₃T_x (6:1) pyrolyzed at 200 °C, which demonstrate a sparse distribution of the Fe-N-C nanoparticles on the outer layer of the Nb₄C₃T_x sheet, leading to the agglomeration and sintering, which would predictably result in the loss of reactivity. Tables S1–2 listed the EDX elemental compositions of the as-prepared electrocatalysts (Supplementary Information, SI).

It is worth mentioning that the Nb₄C₃T_x sheet character is crucial for the circulation of oxygen species inside the materials and regular distributions of the Fe-N-C active sites. Consequently, the first effect kinetically accelerates the electrocatalysis by increasing the flux of reactants and products within the catalyst assembly. The second effect alters the thermodynamics of the catalytic process by creating a greater

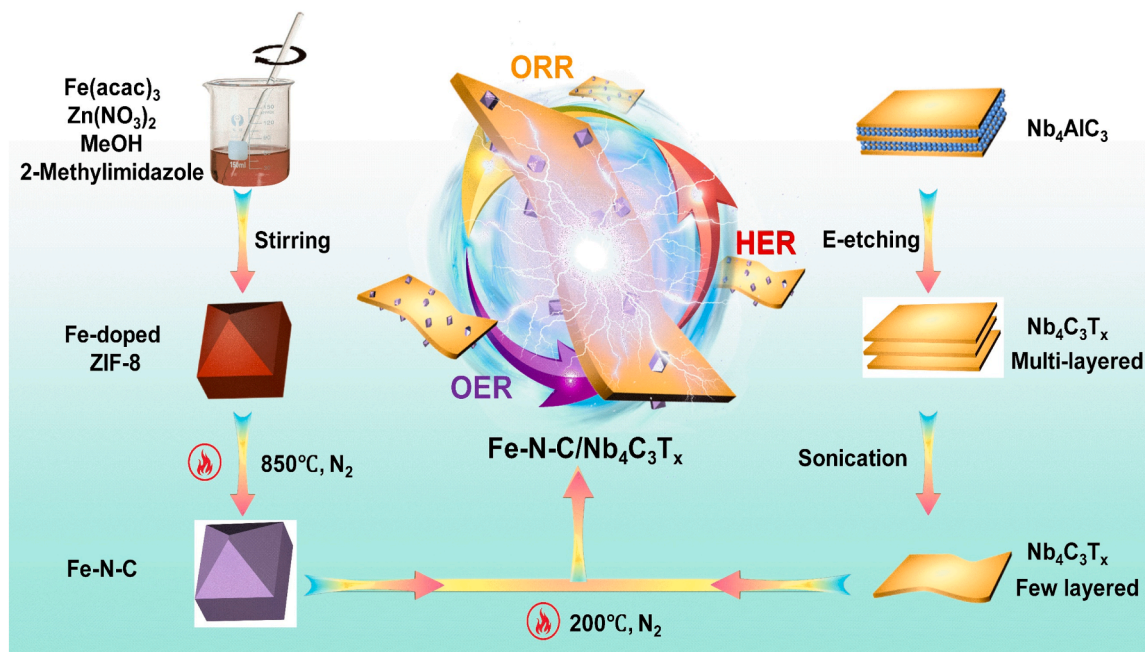


Fig. 1. Schematic illustration of the preparation process for the Fe-N-C/Nb₄C₃T_x.

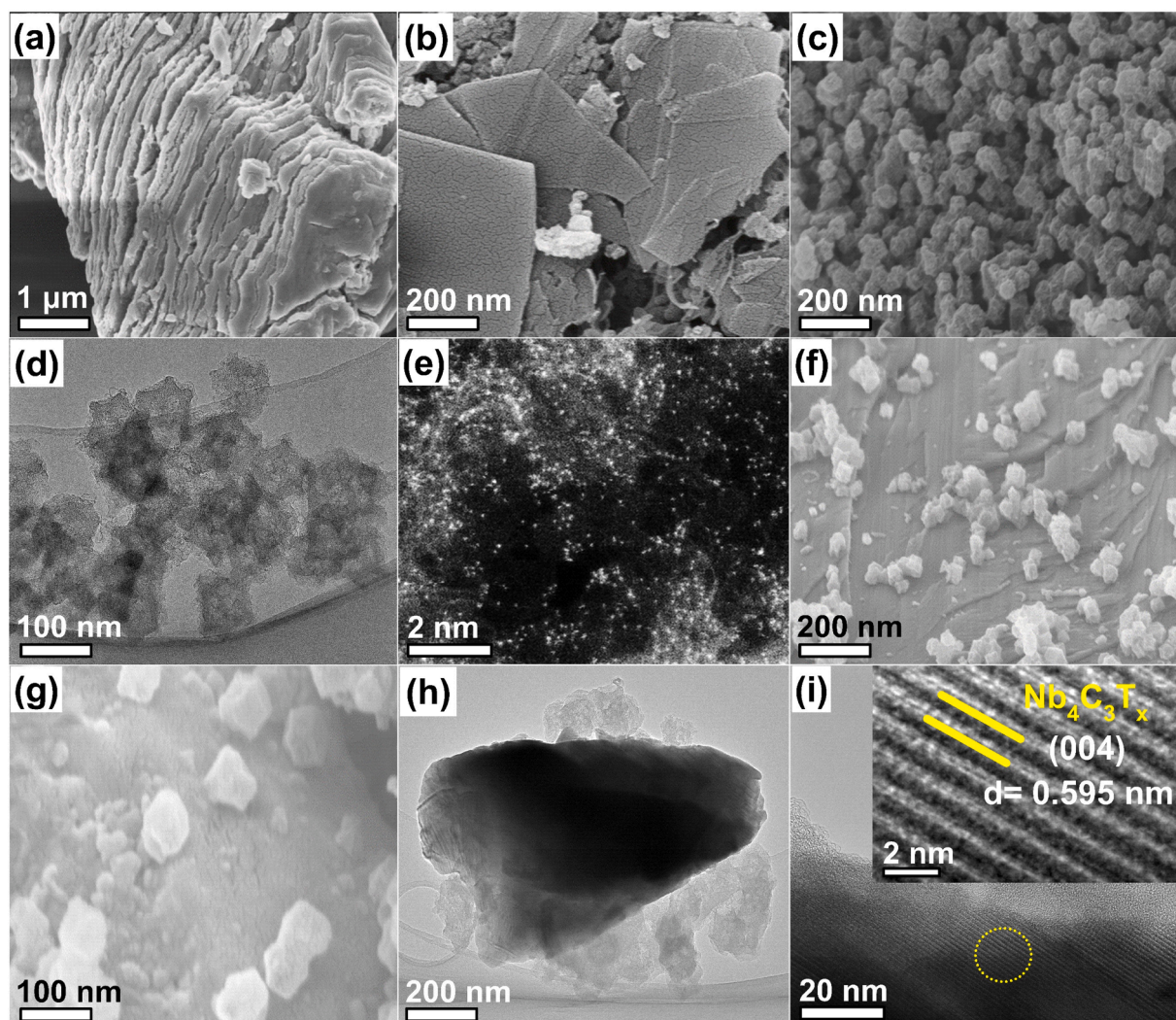


Fig. 2. SEM images of the (a) laminated $\text{Nb}_4\text{C}_3\text{T}_x$, and (b) several-layered $\text{Nb}_4\text{C}_3\text{T}_x$ prepared at an etching potential of 0.6 V. (c) SEM, (d) TEM, and (e) aberration-corrected HAADF-STEM images of Fe-N-C catalyst carbonized at 850 °C. (f–g) Low and high-magnification SEM images, (h) TEM, and (i) HR-TEM images of the Fe-N-C/ $\text{Nb}_4\text{C}_3\text{T}_x$ (2:1)-based catalyst pyrolyzed at 200 °C.

surface area that allows effective contact with the oxygen species. As a result, Fe-N-C/ $\text{Nb}_4\text{C}_3\text{T}_x$ (2:1) would have a higher catalytic activity.

Fig. 3a presents the XRD patterns of the investigated samples, including the Nb_4AlC_3 , $\text{Nb}_4\text{C}_3\text{T}_x$, pristine Fe-N-C, and Fe-N-C/ $\text{Nb}_4\text{C}_3\text{T}_x$. In the XRD pattern of the Fe-N-C, two distinctive peaks at 26.42 and 44.59° align with the (002) and (101) hexagonal crystalline planes of graphitic carbon (JCPDS 01–0646, lattice parameters: $a = b = 2.47 \text{ \AA}$ and $c = 6.80 \text{ \AA}$), indicating a high level of graphitization in this product [40,41]. Additionally, no other peak is detected in this pattern, suggesting only presence of single Fe atoms in the final product.

As the XRD spectrum of Nb_4AlC_3 reveals, the peaks at 14.58, 29.84, 33.39, 35.29, 37.50, 38.31, 40.35, 47.84, 53.42, 54.29, 57.31, 59.10, and 59.68° correspond well to the (004), (008), (101), (103), (0010), (105), (106), (109), (0014), (1011), (1012), (110), and (112) planes of the hexagonal Nb_4AlC_3 (JCPDS: 30–0033), except for the impurity peaks associated with the NbO_2 (JCPDS: 19–0859) and AlNbO_4 (JCPDS: 41–0347), in line with previously reported data [39,42–44]. The presence of such impurities in the Nb_4AlC_3 is mainly attributed to the inevitable oxidation process during the high-temperature processing [42].

Moreover, the XRD spectra of the Nb_4AlC_3 and $\text{Nb}_4\text{C}_3\text{T}_x$ show the characteristic peaks of the (008) and (400) planes, which are initially observed at 29.84° and 30.82°, while disappear after the

electrochemical etching of Nb_4AlC_3 at 0.6 V. These scenarios confirm the successful preparation and delamination of $\text{Nb}_4\text{C}_3\text{T}_x$ -MXene [39,43, 45,46]. Additionally, the XRD pattern of the Fe-N-C/ $\text{Nb}_4\text{C}_3\text{T}_x$ by pyrolysis at 200 °C shows that the distinctive peaks of the $\text{Nb}_4\text{C}_3\text{T}_x$ are still evident upon hybridization with the Fe-N-C, highlighting that the $\text{Nb}_4\text{C}_3\text{T}_x$ -MXene does not disintegrate even with the mild heating treatment [39,46].

To scrutinize the local structural characteristics of the Fe-N-C, advanced X-ray absorption fine structure (XAFS) spectroscopy was implemented, leveraging synchrotron radiation as the probing source. Fig. 3b presented the normalized X-ray absorption near-edge structure (XANES) profiles of the Fe K-edge for the Fe-N-C sample in comparison with relevant counterparts. Notably, the absorption features near the Fe K-edge in the Fe-N-C, which closely resemble those observed in Fe_2O_3 , positioning the energy level between Fe_2O_3 and metallic Fe. This phenomenon suggests a positive valence state ($+0 < \delta < +3$) for the Fe site. Also, the preliminary peak at 7112 eV is attributed to $1s - 4p_z$ orbitals shift, offering compelling evidence of the Fe-N₄ coordination [15,40].

To gain more profound insight into the arrangement of the Fe atoms, we analyzed the Fourier-transformed k^2 -weighted extended X-ray absorption fine structure (EXAFS) spectra within R space. As depicted in Fig. 3c, the prominent peaks at $\sim 1.5 \text{ \AA}$ correspond to the Fe-N interactions. On the contrary, the peaks associated with the Fe-Fe (2.2 \AA)

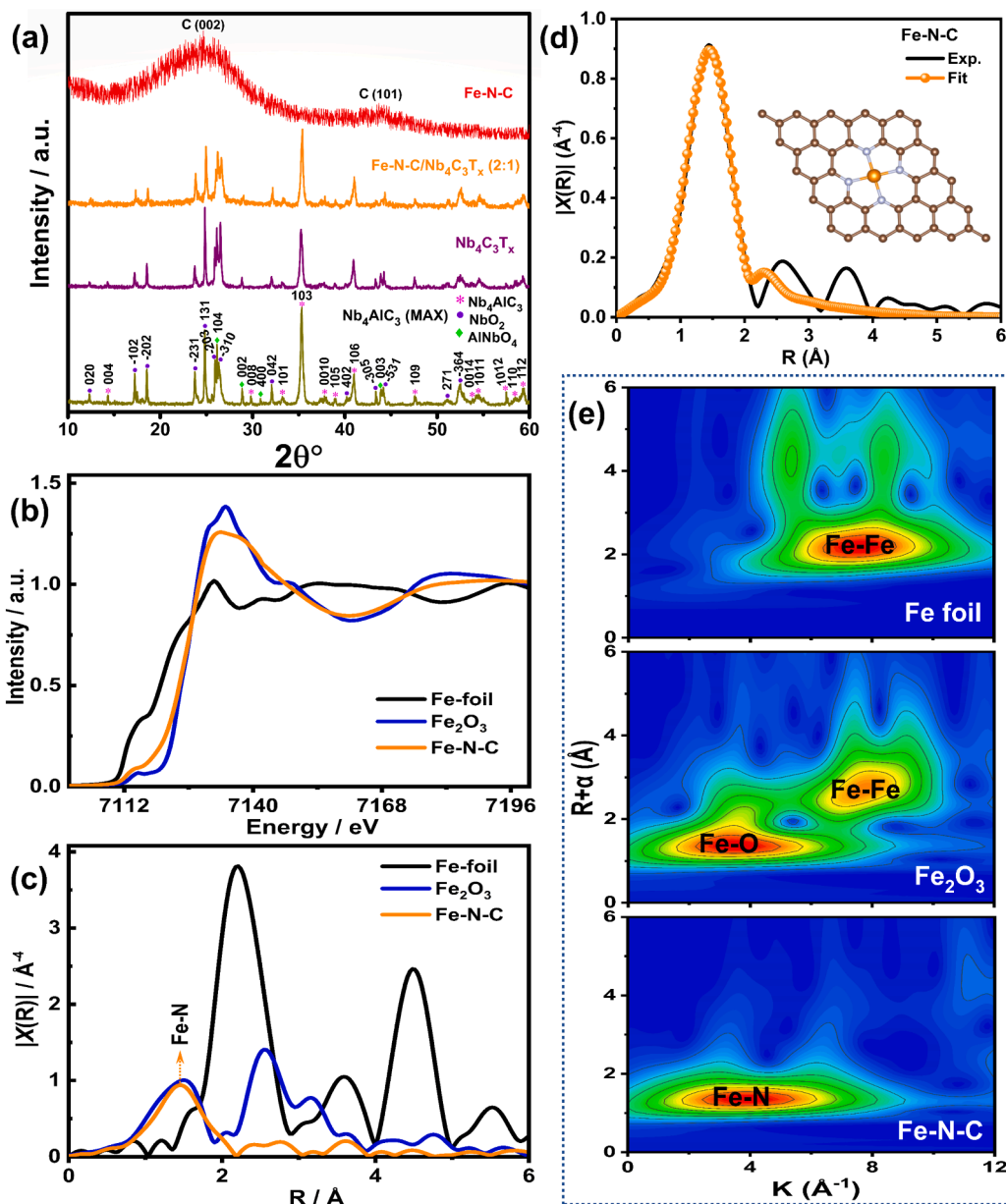


Fig. 3. (a) XRD patterns of the Nb_4AlC_3 , $\text{Nb}_4\text{C}_3\text{T}_x$ prepared at an etching potential of 0.6 V, pristine Fe-N-C carbonized at 850 °C, and Fe-N-C/ $\text{Nb}_4\text{C}_3\text{T}_x$ (2:1) pyrolyzed at 200 °C. Structural analysis based on XAFS; (b) XANES spectra, (c) Fourier-transform (FT) k^2 -weighted EXAFS spectra of Fe-N-C and their reference samples at the Fe K-edge, (d) FT of the k^2 -weighted EXAFS spectra fitting curves of Fe-N-C at the Fe K-edge (inset: structural model of Fe-N-C), and (e) Wavelet transforms of these k^2 -weighted $\chi(k)$ signals of Fe-N-C and reference samples at the Fe K-edge.

scattering path are virtually absent, as observed in the Fe foil reference. These observations suggest that the Fe atoms are atomically distributed within the Fe-N-C configurations.

The Fe atoms within the Fe-N-C were assessed through the least-squares fitting procedures, as illustrated in Fig. 3d and detailed in Table S3. The EXAFS curve-fitting analysis unambiguously assigns the major signal at ~ 1.5 Å to the Fe-N shell coordination. Besides, the EXAFS fitting curve unveils an average Fe coordinated number of roughly 4.2, thus showing a dominating Fe-N_4 configuration in the carbon frameworks [40]. In the structural model of Fe-N_4 , the Fe atom is coordinated with four N atoms.

Fig. 3e provides contour diagrams portraying the k^2 -weighted $\chi(k)$ signals through the utilization of Morlet wavelets characterized by optimal resolution, effectively depicting the outcomes of the wavelet transform (WT). The coordinates (k , R) associated with the intensity maxima in these representations are subject to variations based on the

path length (R) and atomic number (Z). Remarkably, the WT contour diagram is derived from the Fe K-edge analysis of the Fe-N-C, and demonstrates a prominent intensity peak at around 4 Å^{-1} that is definitively linked to the coordination of Fe-N. In contrast to the contour plots of the references, the Fe-N-C sample fails to exhibit any discernible characteristic corresponding to the Fe-Fe or FeO coordination paths. The comprehensive analysis confirms that the Fe-N interactions are prevailing coordination within the Fe-N-C skeleton.

Raman spectroscopy was applied to assess the graphitic features and defects in the samples, as depicted in Fig. 4a. The pristine Fe-N-C and Fe-N-C/ $\text{Nb}_4\text{C}_3\text{T}_x$ samples have two typical peaks at 1342 and 1589 cm^{-1} , which are designated to D-band (defects) and G-band (crystallinity), respectively. It implies that the materials have high crystallinity and abundant defect sites [2,21]. Moreover, the ratios of the peak intensities of the D- to G-band (I_D/I_G) for the pristine Fe-N-C (carbonized at 850 °C), and Fe-N-C/ $\text{Nb}_4\text{C}_3\text{T}_x$ samples with different ratios (i.e., 1:1, 2:1, and 4:1,

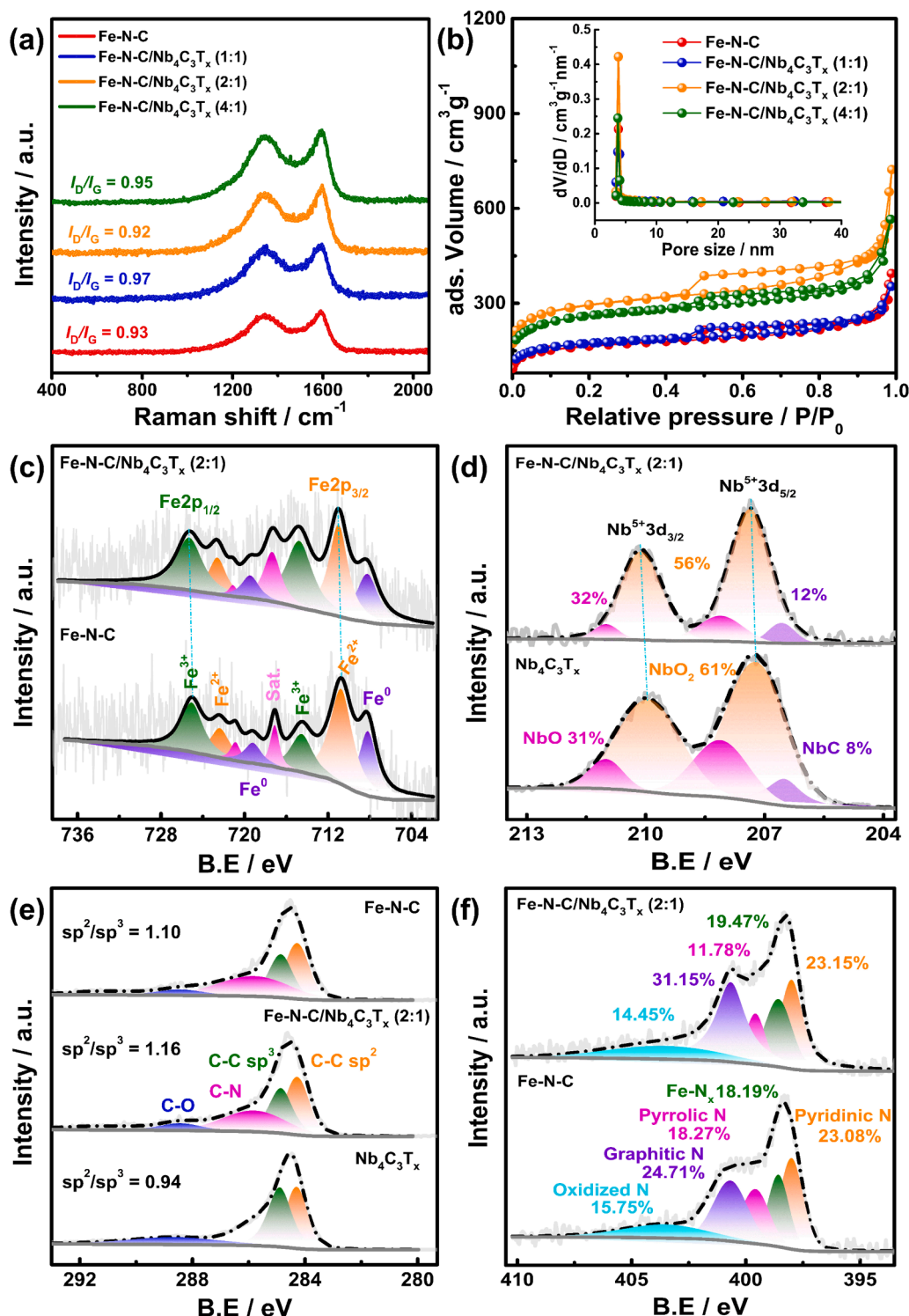


Fig. 4. (a) Raman spectra of the pristine Fe-N-C carbonized at 850 °C, and Fe-N-C/Nb₄C₃T_x with different weight ratios pyrolyzed at 200 °C. (b) The corresponding nitrogen adsorption-desorption isotherms and pore-size-distribution curves. High-resolution (c) Fe 2p, (d) Nb 3d, (e) C 1 s, and (f) N 1 s XPS spectra of the Nb₄C₃T_x, pristine Fe-N-C and the Fe-N-C/Nb₄C₃T_x (2:1).

pyrolyzed at 200 °C) were approximately 0.93, 0.97, 0.92, and 0.95, respectively. The I_D/I_G ratio of the Fe-N-C/Nb₄C₃T_x (2:1) suggests a suitable balance between the defects, graphitization degree, and conductivity, eventually promoting the ORR, OER, and HER activities [47].

Fig. 4b reveals the BET surface porosity of pristine Fe-N-C (carbonized at 850 °C), and Fe-N-C/Nb₄C₃T_x (1:1, 2:1, and 4:1), which was computed from the BJH isotherms acquired under N₂ adsorption/

desorption condition in the relative pressure window (P/P₀) of 0.0–1.0. These findings align with previously reported IV-type isotherms [2], affirming that the investigated materials possess mesoporous properties.

The BET surface areas of the Fe-N-C, Fe-N-C/Nb₄C₃T_x (1:1), Fe-N-C/Nb₄C₃T_x (2:1), and Fe-N-C/Nb₄C₃T_x (4:1) were determined to be 604.32 m²g⁻¹, 645.49 m²g⁻¹, 1083.77 m²g⁻¹, and 943.46 m²g⁻¹, respectively. The significant surface area is attributed to the fact that the

Nb₄C₃T_x sheets create a porous 2D platform that facilitates the even distributions of the Fe-N-C nanoparticles. In contrast, excessive loading of the Fe-N-C nanoparticles accounts for the reduction in the surface area of the Fe-N-C/Nb₄C₃T_x (4:1), causing serious aggregation and sintering that would obstruct or limit the access to the active sites on the Nb₄C₃T_x sheets, thus deteriorating its overall electrocatalytic activity. Additionally, the average pore sizes for the Fe-N-C, and Fe-N-C/Nb₄C₃T_x at different ratios (i.e., 1:1, 2:1 and 4:1) are approximately 4.04 nm, 4.10 nm, 4.12 nm, and 4.13 nm based on the pore-size-distribution graphs, respectively. Besides, the average pore volumes of the Fe-N-C, and Fe-N-C/Nb₄C₃T_x at different ratios (i.e., 1:1, 2:1 and 4:1) are about 0.61, 0.59, 1.12, and 0.87 cm³g⁻¹, respectively. The slight changes in the pore sizes can be attributed to the expansion or contraction (resulted from the phase transformation and thermal stress) during the second pyrolysis treatment. As a result, lots of cracks and voids are formed, subsequently affecting the pore sizes and volumes.

The enlarged surface area and rich mesoporosity of the Fe-N-C/Nb₄C₃T_x (2:1) deliver additional diffusion channels and active sites for the interfacial charge and mass transportation during the electrocatalysis procedures, ultimately improving the ORR, OER, and HER performances [2,4].

XPS assessment was conducted to evaluate the near-surface chemistry (e.g., chemical compositions and valence states) of the Nb₄C₃T_x, Fe-N-C, and Fe-N-C/Nb₄C₃T_x (2:1) catalysts. In the survey XPS spectrum of the Fe-N-C/Nb₄C₃T_x (2:1), discernible signals are identified to the Fe, Nb, C, N, and O elements (Fig. S4a), with the atomic contents of 0.92%, 2.42%, 77.78%, 7.11%, and 11.77%, respectively. These observations align well with the above elemental mapping analysis, offering robust confirmation of the successful synthesis of the Fe-N-C/Nb₄C₃T_x (2:1). Remarkably, the oxygen signals stem from water and oxygen molecules adsorbed on the sample surface [20]. In the high-resolution Fe 2p XPS spectra of the Fe-N-C (Fig. 4c), the Fe 2p signals reveal two distinct sets of subpeaks. According to the spin-orbit splitting of Fe 2p_{3/2}, the peaks at 708.30, 710.80, and 714.53 eV are primarily associated with Fe⁰, Fe²⁺, and Fe³⁺ species, respectively, while those at 719.21, 722.39, and 725.08 eV correspond to Fe⁰, Fe²⁺, and Fe³⁺ species [48,49]. Additionally, notable spikes at 717.14 and 720.87 eV originate from the characteristic satellite peaks [48]. Subsequently, after the incorporation of the Nb₄C₃T_x, both the Fe 2p_{3/2} and Fe 2p_{1/2} peaks in the Fe-N-C/Nb₄C₃T_x undergo the shifts to 711.02 and 725.33 eV with the weaker signals, respectively. The evident shifts in the Fe 2p peaks towards the higher binding energy serve as strong evidence to confirm the robust interactions between the Nb₄C₃T_x and Fe-N-C moiety, eventually showing a substantial reduction in the local electron density of Fe centers.

As seen in Fig. 4d, the Nb 3d segments of the Nb₄C₃T_x exhibit distinct peaks at 207.17 eV and 209.91 eV, primarily corresponding to the Nb 3d_{5/2} and Nb 3d_{3/2} [50]. Concurrently, the other surface compositions were determined as NbC (8%), NbO₂ (61%), and NbO (31%) through the spectral deconvolution [51]. Conversely, both the Nb 3d_{5/2} and Nb 3d_{3/2} peaks display significant upward shifts to 207.37 and 210.10 eV for the Fe-N-C/Nb₄C₃T_x, respectively, confirming robust interactions between the Fe-N-C and Nb₄C₃T_x. The surface compositions of the Fe-N-C/Nb₄C₃T_x are determined as NbC (12%), NbO₂ (56%), and NbO (32%) through spectral deconvolution. The Nb 3d binding energy values, in conjunction with a spin-orbit splitting energy of 3.16 eV, are consistent with the Nb⁵⁺ oxidation state [39,50,51]. Thus, the simultaneous presence of Fe²⁺, Fe³⁺, and Nb⁵⁺ notably indicates that the Fe-N-C/Nb₄C₃T_x surface undergoes oxidation upon exposure to air [52].

The graphitization and defect contents were assessed through the analysis of the C 1s spectra (Fig. 4e). Apparently, the peaks at 284.32 and 284.89 eV correspond to the sp²- and sp³-hybridized carbon [39,53,54], respectively. Upon quantitative analysis, the Fe-N-C/Nb₄C₃T_x exhibits the highest sp²/sp³ ratio of 1.16 as compared to the referenced Fe-N-C (1.10) and Nb₄C₃T_x (0.94). This finding underscores the prevalence of sp² graphitic carbon within the Fe-N-C/Nb₄C₃T_x, aligning well

with the analysis from Raman spectroscopy. Additionally, a discernible peak at 285.89 eV is attributed to the C-N bonds, providing conclusive evidence of N-doping within the carbon matrix. Meanwhile, the peak at 288.47 eV is ascribed to the C-O groups [39,53]. The substantial content of graphitic carbon is significantly beneficial in improving the electrical conductivity, thereby indicating the desired catalytic properties of the Fe-N-C/Nb₄C₃T_x.

In the N 1s XPS spectra of both the Fe-N-C/Nb₄C₃T_x and pure Fe-N-C (Fig. 4f), five distinct peaks emerge at 398.28 eV, 398.93 eV, 399.65 eV, 400.68 eV, and 403.62 eV, corresponding to pyridinic-N, FeN_x, pyrrolic-N, graphitic-N, and oxidized-N species [4], respectively. Notably, the high-density pyridinic-N moiety serves as an electron-attracting group, effectively modulating the intrinsic properties of the catalyst [55]. Besides, the graphitic-N facilitates the cleavage of the O-O bonds, which is a vital process to fortify the carbon matrix and expand the electric conductivity, consequently contributing to the improved performances in both ORR and OER courses [56].

An analysis of the percentage of various nitrogen species reveals that the pyridinic-N and graphitic-N are the dominant configurations in the Fe-N-C/Nb₄C₃T_x and Fe-N-C. It is worth noting that the Fe-N-C/Nb₄C₃T_x unveils the highest Fe-N_x content (19.47 at% of the total nitrogen), which significantly contributes to the heightened electrocatalytic activity. In the O 1s spectral region of the Fe-N-C/Nb₄C₃T_x and Nb₄C₃T_x (Fig. S4b), the prominent peaks at 531.62 eV and 532.59 eV signify the formation of the C-Nb-O_x and C-Nb-(OH)_x bonds. Conversely, the peaks at 530.59 eV and 533.43 eV can be ascribed to impurities (i.e., NbO_x, physically adsorbed water molecules) on the catalyst surface [39].

3.2. Electrochemical performances

The cyclic voltammetry (CV) curves of the assembled Fe-N-C/Nb₄C₃T_x (2:1) were primarily recorded in 0.1 M KOH electrolyte under O₂- or N₂-saturated conditions to evaluate the catalytic properties towards the ORR (Fig. S5a). Obviously, a visible peak is located at 0.79 V in the O₂-saturated surroundings, while disappears in the N₂-saturated environment, reflecting that the Fe-N-C/Nb₄C₃T_x exhibits a strong catalytic efficacy for the ORR [2,53]. To learn more about the ORR properties of the studied catalysts, linear sweep voltammetry (LSV) plots were acquired in the O₂-saturated electrolyte at a scan rate of 5 mV s⁻¹ [57]. Fig. S5b-c shows the LSV curves and Tafel plots of the investigated electrocatalysts prepared by modulating the etching potentials, carbonization, and pyrolysis temperature (see details in Table S4, SI). The Nb₄C₃T_x catalyst (prepared at an etching potential of 0.6 V) shows a positive half-wave potential (*E*_{1/2}) and a significantly higher limiting current density for the ORR, which outperform those prepared by applying the other etching potential (e.g., 0.3 and 0.1 V), mainly attributing to the effective exfoliation of the sheet-like Nb₄AlC₃, as confirmed by the SEM and EDX studies. It is claimed that the organic bond in the zeolitic imidazolate frameworks (ZIFs) and N-doping contents in the home-made catalysts are closely linked to the catalytic activity, which can be altered by the carbonization [15,31]. Thus, the Fe-N-C sample carbonized at 850 °C reflects the most positive *E*_{1/2} and the maximum limiting current density when compared to those carbonized at 600 and 1000 °C, primarily due to the main degradation of the organic bonds in the ZIFs below 900 °C [15].

The impact of the 2nd pyrolytic temperature on the ORR performance was also explored under this premise, while the weight ratio of the Fe-N-C to Nb₄C₃T_x was fixed at 2:1 and the carbonization temperature was set at 850 °C for the Fe-N-C. Notably, the Fe-N-C/Nb₄C₃T_x samples exhibit an upward trend towards the catalytic characteristics as the pyrolysis temperature rises up to 200 °C, while the ORR activities and kinetics experience a decline over this temperature. These observations are resulted from the decomposition of the Nb₄C₃T_x into CO, CO₂ and NbO₂ through oxidation when the temperature is elevated. Such decomposition is detrimental to the conductivity of the Nb₄C₃T_x substrate (exclusion of ⁻OH and ⁺H from the surface), along with the

decline in the active sites [31,39]. As a result, the optimal conditions include an etching potential of 0.6 V, carbonization at 850 °C and 200 °C for the standard production of the Fe-N-C/Nb₄C₃T_x (2:1).

As shown in Fig. 5a, the Fe-N-C/Nb₄C₃T_x (2:1) exhibits the most desired ORR behavior, with a highly favorable onset potential ($E_{\text{Onset}} = 1.022$ V vs. RHE) and $E_{1/2}$ of 0.911 V (vs. RHE) as compared to the Pt/C ($E_{\text{Onset}} = 0.966$ V; $E_{1/2} = 0.824$ V), outperforming the referenced Nb₄C₃T_x ($E_{\text{Onset}} = 0.876$ V; $E_{1/2} = 0.742$ V), pristine Fe-N-C ($E_{\text{Onset}} = 1.002$ V; $E_{1/2} = 0.883$ V), Fe-N-C/Nb₄C₃T_x (1:1) ($E_{\text{Onset}} = 1.002$ V; $E_{1/2} = 0.876$ V), and Fe-N-C/Nb₄C₃T_x (4:1) ($E_{\text{Onset}} = 1.009$ V; $E_{1/2} = 0.904$ V).

Notably, the effects of the ratios between the Fe-N-C and Nb₄C₃T_x on the electrocatalytic properties clearly show that the 1:1 ratio gives the worst ORR activity, coupled by exhibiting the weakest ORR response for the Nb₄C₃T_x itself. At the higher Fe-N-C ratios (e.g., 3:1, 4:1, and 6:1), there show the severer agglomeration and sintering behavior of the Fe-N-C particles on the Nb₄C₃T_x substrate. Consequently, the active surface

area is decreased, subsequently diminishing the ORR catalytic activity (Fig. S5b-c, Table S4). Thus, we reasonably conclude that the optimized Fe-N-C/Nb₄C₃T_x (2:1) exhibits the most favorable E_{Onset} and $E_{1/2}$, due to its ability to maintain a high specific surface area, mitigate agglomeration, and provide the most favorable equilibrium between the Fe-N-C and Nb₄C₃T_x.

Moreover, the Fe-N-C/Nb₄C₃T_x (2:1) exhibits the maximum limiting current density of -6.909 mA cm⁻² at 0.20 V for the ORR, in contrast to the control Pt/C under the same settings. These observations are resulted from the exceptional conductive channel provided by the Nb₄C₃T_x sheets and more active sites created by the deposited Fe-N-C nanoparticles [28,31].

The Tafel plot of a catalyst is often used to explore the ORR kinetics from the LSV curves [4]. As Fig. 5b illustrates, the Tafel slope of the Fe-N-C/Nb₄C₃T_x (2:1) is about 70.08 mV dec⁻¹, which is substantially lower when compared to those of Pt/C (96.89 mV dec⁻¹), Nb₄C₃T_x (87.66 mV dec⁻¹), pristine Fe-N-C (74.08 mV dec⁻¹), Fe-N-C/Nb₄C₃T_x

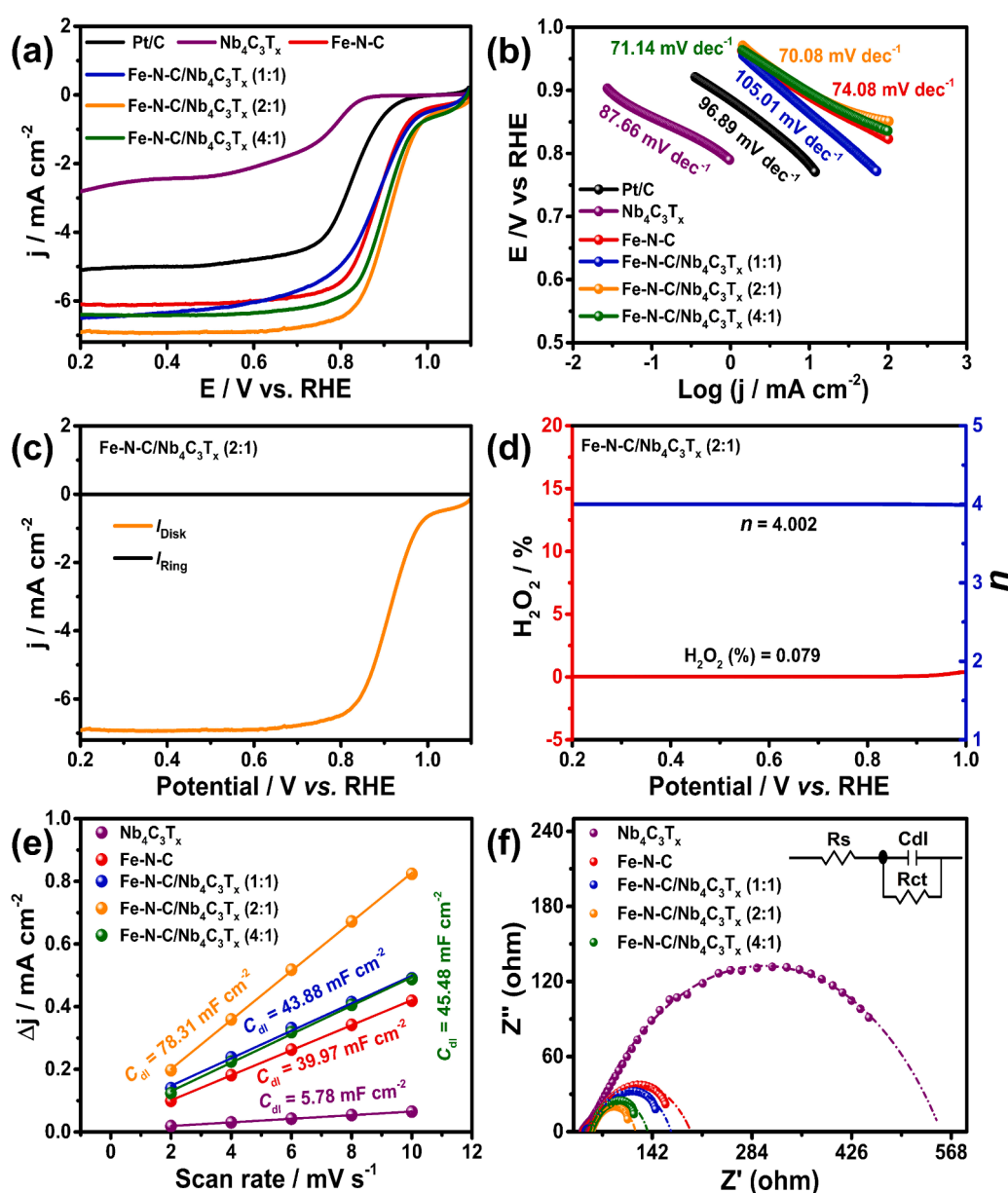


Fig. 5. (a) LSV curves and (b) Tafel plots of the as-prepared catalysts and control Pt/C in the O₂-saturated 0.1 M KOH solution at 1600 rpm at 5 mV s⁻¹ for the ORR. (c) The ORR polarization curves of the Fe-N-C/Nb₄C₃T_x (2:1) recorded on the RRDE at the rotation rate of 1600 rpm. (d) The related H₂O₂ yield, n values, and (e) C_{dl} values derived from the CV curves at different scan rates. (f) The Nyquist plots of the as-prepared catalysts (equivalent Randle's circuit fitting).

(1:1) (105.01 mV dec⁻¹), and Fe-N-C/Nb₄C₃T_x (4:1) (71.14 mV dec⁻¹). It demonstrates the substantial increase in the ORR kinetics for the Fe-N-C/Nb₄C₃T_x (2:1) in comparison with other metal-carbides and nitrides reported earlier (see details in Table 1) [2,4,19,28,39,57–62]. The strong ORR characteristics of the Fe-N-C/Nb₄C₃T_x (2:1) is primarily ascribed to the bulky specific surface area, graded porous structure, appropriate graphitization degree, compositional synergy, and the effects of coordinative electron-rich metal ions [4,28,39].

The chemical kinetics of the electrocatalysts were analyzed on the rotating ring-disk electrode (RRDE) [2]. Fig. 5c–d shows the hydrogen peroxide yield [H₂O₂ (%)] and number of electron transfer (*n*) of the Fe-N-C/Nb₄C₃T_x (2:1). Briefly, the average *n* of the Fe-N-C/Nb₄C₃T_x (2:1) is about 4.002, confirming that the ORR follows the direct four-electron route with a low H₂O₂ (%) of 0.079% in the specified potential window. Likewise, Fig. S5d–f illustrates that the *n* and H₂O₂ (%) values on the pristine Fe-N-C (3.978 and 1.337%), Fe-N-C/Nb₄C₃T_x (1:1) (3.985 and 1.096%), and Fe-N-C/Nb₄C₃T_x (4:1) (3.996 and 0.852%), further showing the four-electron pathway of the ORR at the catalyst surfaces [2,19].

The electrochemical active surface area (ECSA) shows a direct influence on the ORR, which can be assessed by double-layer capacitance (*C_{dl}*) derived from the CV curves (Fig. S6a–e) [39]. As Fig. 5e depicts, the Fe-N-C/Nb₄C₃T_x (2:1) exhibits a higher *C_{dl}* value of 78.31 mF cm⁻² relative to other investigated catalysts, including the Nb₄C₃T_x (5.78 mF cm⁻²), Fe-N-C (39.97 mF cm⁻²), Fe-N-C/Nb₄C₃T_x (1:1) (43.88 mF cm⁻²), and Fe-N-C/Nb₄C₃T_x (4:1) (45.48 mF cm⁻²). These data reflect that the well-organized porous structure of the Fe-N-C/Nb₄C₃T_x accounts for a substantial increase in the active sites required to enhance the electrocatalytic reactions ultimately [31,39].

Electrochemical impedance spectroscopy was employed to elaborate the above phenomena more clearly by the acquired Nyquist plots with curve fitting parameters derived from the equivalent Randle's circuit fitting protocol (Fig. 5f) [2,63]. The Fe-N-C/Nb₄C₃T_x (2:1) grants the smallest arc with the least charge-transfer resistance (*R_{ct}* = 48.15 Ω), reflecting the high electronic conductivity among the other investigated catalysts (Table S5). As a result, the highest ORR kinetics is realized, which is consistent with the above investigations. The prolonged conjugated π–π* electron configuration and synergistic interactions between the Fe-N-C and Nb₄C₃T_x are principally responsible for the strong

charge-transfer capability of the Fe-N-C/Nb₄C₃T_x [2,39].

Long-term stability is also an imperative factor in determining the feasibility of advanced catalysts in practice [19]. As Fig. 6a displays, the Fe-N-C/Nb₄C₃T_x (2:1) presents a small shift of the *E*_{1/2} (4 mV) in the negative direction by continuously scanning for 2000 cycles, in contrast to the typical Pt/C (20 mV), thereby confirming the exceptional stability.

Similarly, the chronoamperometry test was run for 10 h by applying a potential of 0.6 V with a rotation speed of 1600 rpm to investigate the long-lasting durability (Fig. 6b). The Fe-N-C/Nb₄C₃T_x (2:1) shows that the current density retained 93.7% of its original value after the 10-h test, outperforming the Pt/C (62.9%) in the same settings, confirming the excellent stability. As a promising replacement for the carbon-based substrate, the incredible durability of the Fe-N-C/Nb₄C₃T_x (2:1) is predominantly owed to the excellent electronic channels and minimal aggregation of coarse Fe-N-C nanoparticles well dispersed on the Nb₄C₃T_x sheets [4,19].

Finally, methanol tolerance is critical because the ORR is a fundamental half-reaction in the methanol fuel cells [28]. Contrary to the Pt/C, the Fe-N-C/Nb₄C₃T_x (2:1) displays almost constant chronoamperometric responses before and after the infusion of methanol (1.0 M) at 300 s (Fig. S6f), highlighting the tremendous methanol resistance in this study. As a result of its compelling ORR catalytic features and high methanol tolerance, the Fe-N-C/Nb₄C₃T_x (2:1) is intended to play a major role in zinc-air batteries.

The OER is a rate-determining step in metal-air batteries and water-electrolysis devices [4,60]. The LSV plots were acquired to probe the OER characteristics of the investigated electrocatalysts in a 1.0 M KOH electrolyte at 5 mV s⁻¹. As seen in Fig. 6c, the Fe-N-C/Nb₄C₃T_x (2:1) achieves a current density of 10 mA cm⁻² at an overpotential (*η*₁₀) of 1.52 V, which is comparable to RuO₂ (1.49 V), but much lower than the other catalysts such as Ni foam (*η*₁₀ = 1.67 V), Nb₄C₃T_x (*η*₁₀ = 1.65 V), pristine Fe-N-C (*η*₁₀ = 1.60 V), Fe-N-C/Nb₄C₃T_x (1:1) (*η*₁₀ = 1.58 V), and Fe-N-C/Nb₄C₃T_x (4:1) (*η*₁₀ = 1.57 V), coupled by outperforming other metal-carbides and nitrides reported earlier (Table 2) [2,4,19,28,39,58, 60–69]. The slight overpotential of the Fe-N-C/Nb₄C₃T_x (2:1) over previous electrocatalysts is mainly ascribed to the significant coupling and synergistic interactions among the Fe-N-C nanoparticles and the Nb₄C₃T_x sheets [2,28].

Further, the Tafel curves were employed to characterize the OER kinetics [60]. As depicted in Fig. 6d, the Fe-N-C/Nb₄C₃T_x (2:1) grants the slightest Tafel slope of 42.44 mV dec⁻¹ in contrast to the RuO₂ (57.20 mV dec⁻¹), Ni foam (49.60 mV dec⁻¹), Nb₄C₃T_x (48.96 mV dec⁻¹), Fe-N-C (63.83 mV dec⁻¹), Fe-N-C/Nb₄C₃T_x (1:1) (61.63 mV dec⁻¹), and Fe-N-C/Nb₄C₃T_x (4:1) (60.08 mV dec⁻¹). It indicates the feasibility of the Fe-N-C/Nb₄C₃T_x (2:1) due to its faster OER kinetics than the other studied catalysts.

The impressive OER kinetics of the Fe-N-C/Nb₄C₃T_x (2:1) is primarily linked to the increased surface area and high porosity, which affords a substantial number of active sites and interconnected channels for the interfacial mass circulation and electron transport, which would facilitate the OER activity in this scenario [28].

Moreover, stability of a catalyst is essential to assess its potential use in practice. As depicted in Fig. 7a, the LSV curves of the Fe-N-C/Nb₄C₃T_x (2:1) almost remain similar to the initial curve even after undergoing 2000 cycles, with only minor changes in the current densities and overpotential (*η*₁₀ = 1.54 V). This observation underscores a significant improvement in its stability. Additionally, Fig. 7b provides further evidence for the superior stability, as it shows consistent and stable current densities throughout the corresponding chronoamperometric test operated for 12 h at 10 mA cm⁻². Notably, there hardly shows any significant fluctuation in the current density, highlighting the robust and long-lasting performance of the catalyst.

As aforementioned, the Fe-N-C/Nb₄C₃T_x contains Fe³⁺ and Nb⁵⁺ species. During the initial stages of the OER, substantial amounts of the Fe³⁺ and Nb⁵⁺ species in the catalyst provide a higher density of active

Table 1

Comparison of the ORR, OER, HER and water splitting performances of the investigated catalysts with other metal carbides- and nitrides-based electrocatalysts.

Catalysts	<i>E</i> _{1/2}	<i>η</i> @ 10 mA cm ⁻²			Refs.
	ORR (V)	OER (V)	HER (mV)	WS (V)	
Fe-N-C/Nb ₄ C ₃ T _x (2:1)	0.911	1.52	91	1.58	This work
N-CoSe ₂ /3D Ti ₃ C ₂ T _x	0.79	1.54	N/A		2
CoS ₂ @MXene	0.80	1.50	175	1.62	4
Co ₂ P/CoN- NCNTs	0.85	1.65	N/A		19
Fe/Co-CNT@MXene	0.85	1.59	N/A		28
Nb ₂ CO ₂ @COFs	0.81	1.603	N/A		39
Mn ₃ O ₄ /MXene	0.70	N/A	N/A		57
Co/N-CNTs@ Ti ₃ C ₂ T _x	0.81	1.641	N/A		58
Pd/Ti ₃ C ₂ T _x -CNT	0.92	NA	330		59
NiCo ₂ O ₄ /MXene	0.70	1.54	N/A		60
NiCoS ₂ /Ti ₃ C ₂ T _x	N/A	1.595	N/A		61
Nitride/N-Ti ₃ C ₂	0.84	1.53	N/A		62
CoP @ 3D MXene	N/A	1.64	168	1.58	64
Ni _{0.9} Fe _{0.1} PS ₃ @MXene	N/A	1.512	198	1.65	65
MWCNT/V ₂ CT _x	N/A	1.699	27		66
Co ³⁺ -Ti ₂ CT _x	N/A	1.655	460		67
Ni-MoSe ₂ @MXene	N/A	1.50	92	1.59	68
BP QDs@Ti ₃ C ₂ T _x	N/A	1.59	190	1.78	69

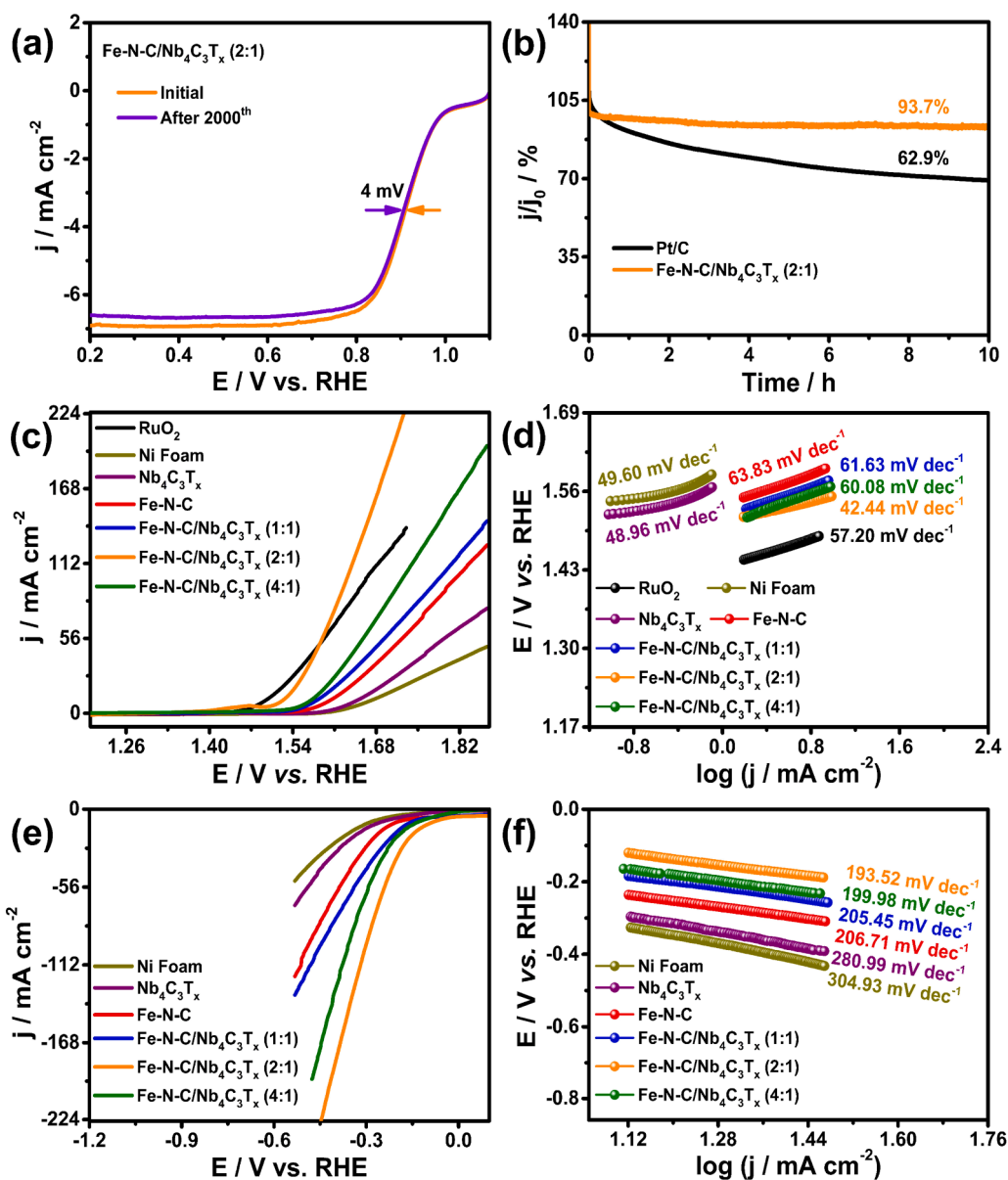


Fig. 6. (a) ORR curves of the Fe-N-C/Nb₄C₃T_x (2:1) before and after sweeping for 2000 cycles at 10 mV s⁻¹. (b) Chronoamperometric curves of the catalyst based on the Fe-N-C/Nb₄C₃T_x (2:1) and control Pt/C measured at 0.6 V with a rotation rate of 1600 rpm. (c) LSV curves and (d) Tafel plots of the as-prepared catalysts and control RuO₂ in a 1.0 M KOH solution at 5 mV s⁻¹ for the OER. (e) LSV curves and (f) Tafel plots of the as-prepared catalysts for the HER.

Table 2

Comparison of the performances of the as-developed Zn-air battery with other metal carbides, nitrides and oxide-based electrocatalysts.

Catalysts	VOC (V)	PD (mW cm ⁻²)	VP	Stability (h)	Refs.
Fe-N-C/Nb ₄ C ₃ T _x (2:1)	1.51	136	0.85 V @ 5 mA cm ⁻²	20 min/cycle for 660 cycles; 220 h	This work
N-CoSe ₂ /3D Ti ₃ C ₂ T _x	1.43	142	0.82 V @ 10 mA cm ⁻²	20 min/cycle for 500 cycles; 166 h	2
CoS ₂ @MXene	1.45	~30	~0.53 V @ 1 mA cm ⁻²	20 min/cycle for 60 cycles; 20 h	4
Co ₂ P/CoN-NCNTs	1.362	196.4	0.76 V @ 5 mA cm ⁻²	60 min/cycle for 96 cycles; 96 h	19
Fe@C-NG/NCNTs	1.37	101.3	0.89 V @ 10 mA cm ⁻²	20 min/cycle for 297 cycles; 99 h	21
Fe/Co-CNT@MXene	1.41	138	0.77 V @ 10 mA cm ⁻²	20 min/cycle for 1000 cycles; 350 h	28
Nb ₂ CO ₂ @COFs	1.418	75	-	20 min/cycle for 360 cycles; 120 h	39
NiCo ₂ O ₄ /MXene	1.40	277	0.9 V @ 5 mA cm ⁻²	20 min/cycle for 1000 cycles; 333 h	60
NiCoS/Ti ₃ C ₂ T _x	1.43	-	0.70 V @ 50 mA cm ⁻²	8 h	61
Nitride/N-Ti ₃ C ₂	1.495	-	-	60 min/cycle for 120 cycles; 120 h	62
Co/Co _x M _y + Pt/C	1.425	125.2	0.91 V @ 10 mA cm ⁻²	20 min/cycle for 500 cycles; 166 h	70
FePc@N,P-DC	1.45	120	0.50 V @ 2 mA cm ⁻²	200 s/cycle for 900 cycles; 50 h	71

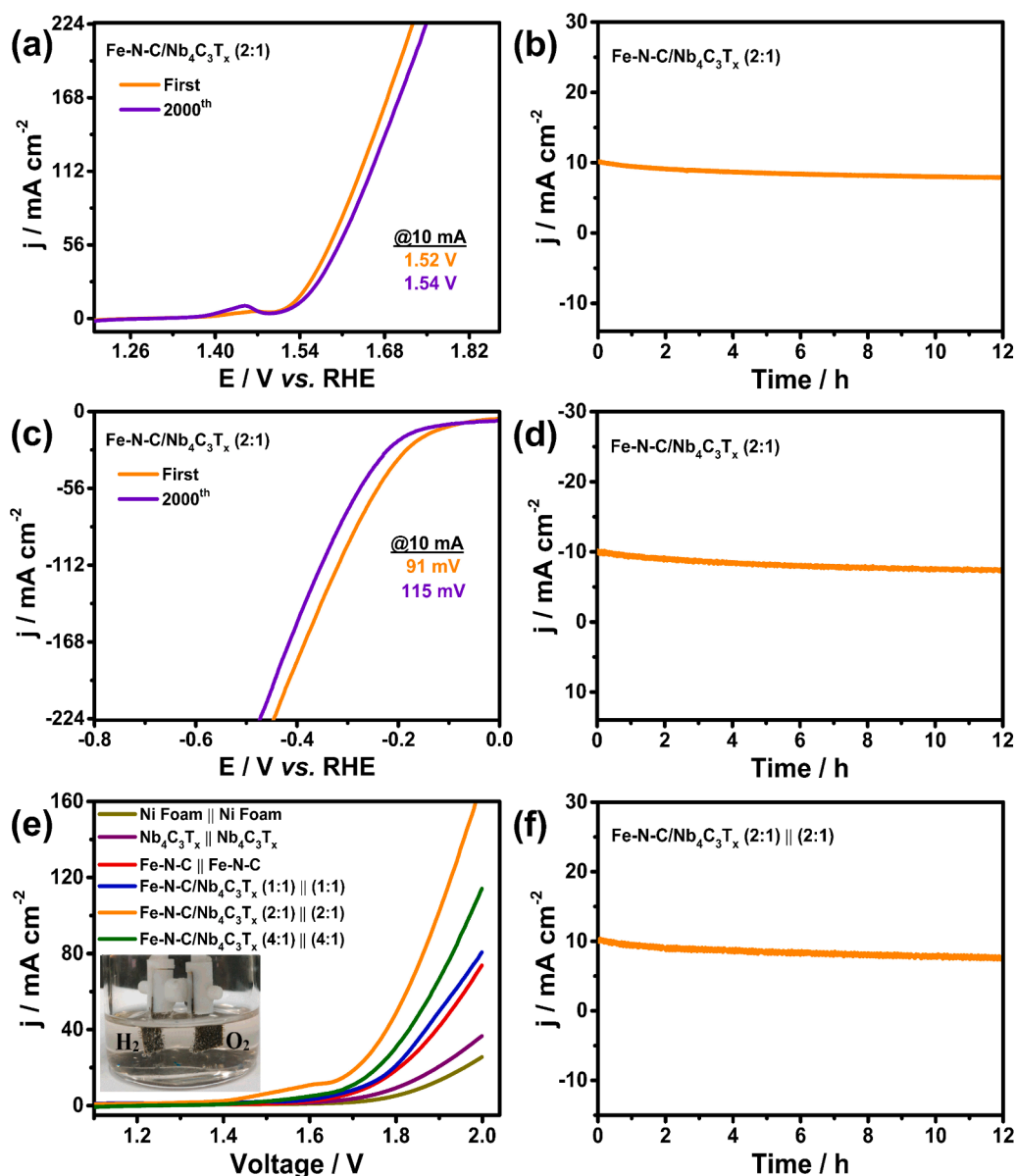


Fig. 7. (a) OER curves of the Fe-N-C/Nb₄C₃T_x (2:1) before and after sweeping for 2000 cycles at 10 mV s⁻¹, and (b) the chronoamperometric curve at the current density of 10 mA cm⁻². (c) HER curves of the Fe-N-C/Nb₄C₃T_x (2:1) before and after sweeping for 2000 cycles at 10 mV s⁻¹, and (d) the chronoamperometric curve at 10 mA cm⁻². (e) LSV curves for overall water splitting by using the Fe-N-C/Nb₄C₃T_x as both anodic and cathodic catalysts in the 1.0 M KOH circumstance (Inset shows the respective photograph for producing H₂ and O₂ bubbles), and (f) chronoamperometric curve of the Fe-N-C/Nb₄C₃T_x (2:1) based water electrolysis at 1.58 V for 12 h.

sites during the water adsorption and dissociation processes [28,39]. At the same time, the hierarchical structure and incorporated N atoms into the metal core activate the electronic states of graphitic carbon, resulting in a higher proportion of oxygen vacancies. This feature proves beneficial for the adsorption of OOH* species, ultimately enhancing the reactivity of the OER [39,48].

Beyond the above, the investigated catalysts also have the higher electrocatalytic HER activity in the same setting, which is required for its application in the water-splitting devices [64,65]. The LSV curves were used to probe the HER characteristics of the studied catalysts in a 1.0 M KOH solution at 5 mV s⁻¹. As Fig. 6e shows, the Fe-N-C/Nb₄C₃T_x (2:1) provides the smaller overpotential (η_{10} = 91 mV) to accomplish the fixed current density of 10 mA cm⁻², which is much lower compared to those of Ni foam (η_{10} = 295 mV), Nb₄C₃T_x (η_{10} = 273 mV), Fe-N-C (η_{10} = 209 mV), Fe-N-C/Nb₄C₃T_x (1:1) (η_{10} = 160 mV), and Fe-N-C/Nb₄C₃T_x (4:1) (η_{10} = 140 mV), and also outperforms the previously reported

MXene-based catalysts (Table 1) [4,59,64–69]. It means ideal HER occurred on the Fe-N-C/Nb₄C₃T_x (2:1) in this context.

The improved HER characteristics of the Fe-N-C/Nb₄C₃T_x are predominantly recognized to the synergistic contacts of the Nb₄C₃T_x sheets with Fe-N-C nanoparticles, rich oxygen defects, and the active sites produced by activating the electronic states of carbon via N-doping the metal core. These factors are crucial for ions transfer and H₂ overflow to increase the HER activity [59,65].

Besides, the Tafel slopes were extensively examined for having deep information about the HER kinetics [64]. As exposed in Fig. 6f, the Fe-N-C/Nb₄C₃T_x (2:1) presents the slightest Tafel slope of 193.52 mV dec⁻¹ in comparison to the Ni foam (304.93 mV dec⁻¹), Nb₄C₃T_x (280.99 mV dec⁻¹), Fe-N-C (206.71 mV dec⁻¹), Fe-N-C/Nb₄C₃T_x (1:1) (205.45 mV dec⁻¹), and Fe-N-C/Nb₄C₃T_x (4:1) (199.98 mV dec⁻¹). It indicates that the HER on the Fe-N-C/Nb₄C₃T_x (2:1) undergoes a strong Volmer-Heyrovsky reaction (H₂O + e → H* + OH⁻) [31]. Obviously, the

enhanced HER kinetics is concerned with the strong adsorption and rapid dissociation of water molecules, which significantly speeds up the Tafel steps through the high coverage of H_{ads} on the catalyst surface in the basic electrolyte, thereby boosting the HER activity [4,59].

The durability test is critical for assessing the prolonged stability of the Fe-N-C/Nb₄C₃T_x (2:1). The corresponding LSV curve closely resembles the initial curve even after undergoing 2000 cycles (Fig. 7c), with only minor changes in the current densities and overpotential ($\eta_{10} = 115$ mV). This outcome highlights a noteworthy enhancement in the stability. Also, the chronoamperometric plots (Fig. 7d) demonstrate that the Fe-N-C/Nb₄C₃T_x maintains a nearly constant current density of 10 mA cm^{-2} throughout the operational period of 12 h. The negligible decline in the current density over this extended course provides compelling evidence for the substantial enhancement in the catalyst's stability. Thus, the exceptional ORR, OER and HER characteristics of the Fe-N-C/Nb₄C₃T_x (2:1) are primarily attributed to their extremely high surface-volume proportion and porous nature, emphasizing a high density of active sites during the electrocatalysis procedures.

3.3. Performance of overall water splitting

Due to the superior catalytic properties of the investigated catalysts, an electrolyzer with a two-electrode configuration was constructed for the complete water splitting in a 1.0 M KOH electrolyte. In this setup, the catalysts were loaded onto the Ni foams that served as both the cathode and anode, while bare Ni foam was behaved as a reference. As shown in Fig. 7e, the Fe-N-C/Nb₄C₃T_x (2:1)||Fe-N-C/Nb₄C₃T_x (2:1) combination requires a cell potential of 1.58 V to achieve a current density of 10 mA cm^{-2} , which is lower than those of bare Ni foam (1.86 V), Nb₄C₃T_x (1.80 V), Fe-N-C (1.73 V), Fe-N-C/Nb₄C₃T_x (1:1, 1.72 V), and Fe-N-C/Nb₄C₃T_x (4:1, 1.69 V) under similar conditions. Notably, the catalytic efficacy of the Fe-N-C/Nb₄C₃T_x (2:1)-based configuration proves to be on par with that of early water-splitting catalysts, as detailed in Table 1 [4,64,65,68,69].

Inset in Fig. 7e shows a digital image of the Fe-N-C/Nb₄C₃T_x (2:1) water splitting device, where abundant gas bubbles show up on the Ni foam, indicating the high efficiency of the overall water splitting system. Further, the relevant durability was scrutinously assessed by chronoamperometry at 1.58 V (Fig. 7f). Evidently, the current densities

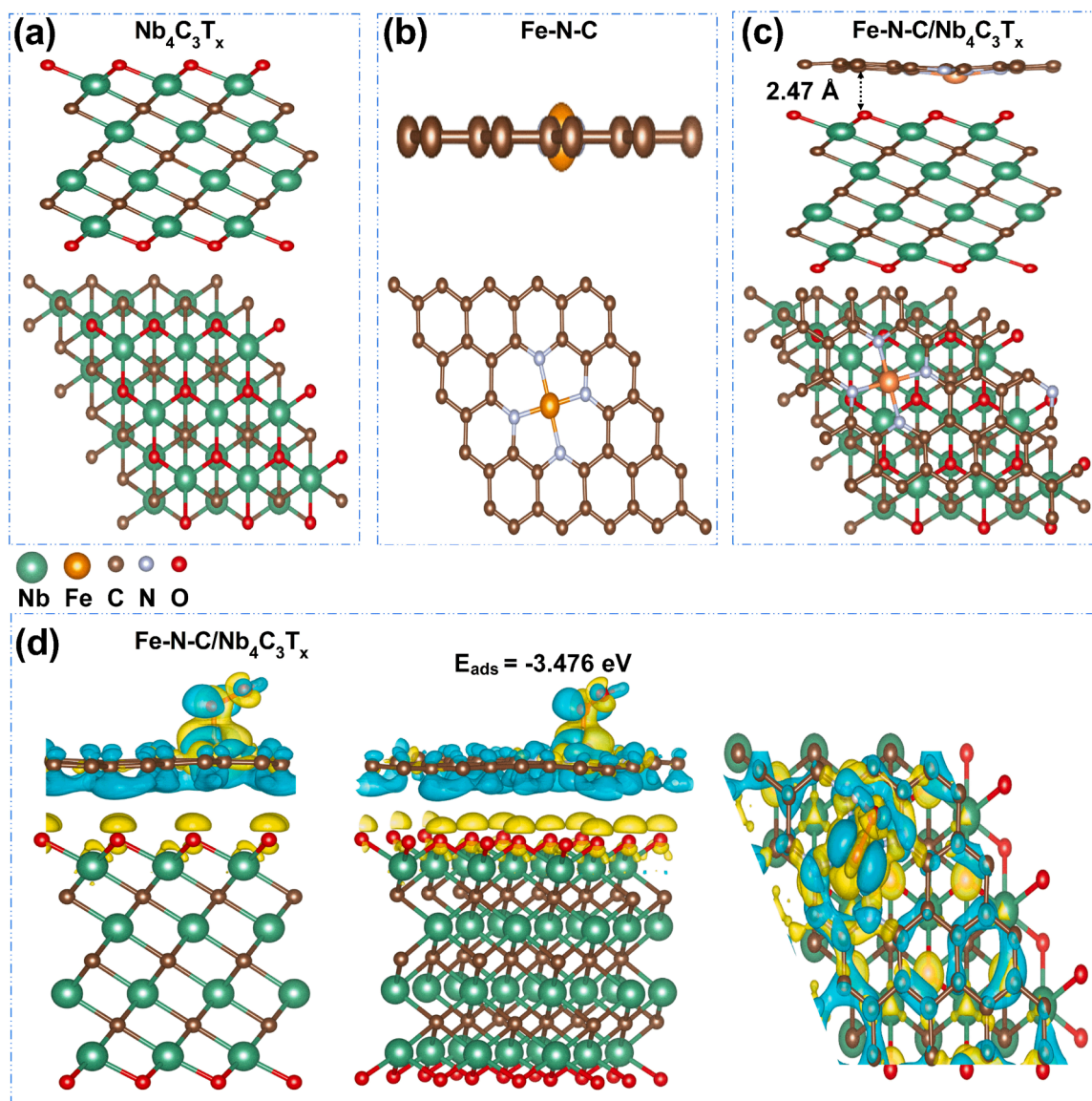


Fig. 8. Structural optimization of the (a) Nb₄C₃T_x, (b) Fe-N-C, and (c) Fe-N-C/Nb₄C₃T_x catalysts. (d) Differential electron density diagram of Fe-N-C/Nb₄C₃T_x (Aqua green and yellow colors represent electron depletion and electron accumulation with the iso-surface value of 0.002 e/Bohr^3).

remain nearly constant for the Fe-N-C/Nb₄C₃T_x (2:1) over a testing period of 12 h, highlighting its exceptional stability.

3.4. DFT calculations

Utilizing the exceptional catalytic properties of the Fe-N-C/Nb₄C₃T_x in terms of the ORR, OER, and HER, we embarked on a comprehensive theoretical investigation. Our initial step involved structural optimization of the Fe-N-C/Nb₄C₃T_x with the VASP package. Both the Fe-N-C and Nb₄C₃T_x belong to the hexagonal crystal system. For calculations, we employed a Monkhorst-Pack grid of $2 \times 2 \times 1$ k-point sampling for isolated Fe-N-C and Nb₄C₃T_x, as well as the heterostructured Fe-N-C/Nb₄C₃T_x.

The Nb₄C₃T_x slab model utilized a supercell containing 36 Nb atoms, 27 C atoms, and 18 O atoms (Fig. 8a), with a vacuum layer of 20 Å. Likewise, the Fe-N-C slab model was established by using a supercell containing 26 C atoms, 4 N atoms, and one Fe atom to separate the slabs along the z-direction (Fig. 8b), with the same vacuum layer (20 Å). For construction of the Fe-N-C/Nb₄C₃T_x heterostructure, a relaxed monolayer of Fe-N-C was stacked directly above a monolayer of Nb₄C₃T_x. This heterostructural model employed a supercell containing 36 Nb atoms, 53 C atoms, 18 O atoms, 4 N atoms, and one Fe atom (Fig. 8c), with the identical vacuum layer (20 Å). The distance between the Fe-N-C and Nb₄C₃T_x was approximately 2.47 Å.

Subsequently, the electronic structure calculations and free energy assessments for the OH*, O*, OOH*, and H* on the substrate surface were conducted with the VASP package. Fig. S7 illustrates the selection of the most stable adsorption sites based on the principle of the minimal energy for oxygen or hydrogen on the material, as summarized in Table S6. For the isolated Fe-N-C and Fe-N-C/Nb₄C₃T_x heterostructure, the representative adsorption patterns I, II and III show the adsorbent atoms directly above the Fe, C and N atoms, respectively. In the controlled Nb₄C₃T_x, the adsorbent atoms were positioned above the Nb,

C, and O atoms. The most stable adsorption sites for the O and H atoms were above the Nb atoms (Pattern IV) and O atoms (Pattern VI), respectively.

Fig. 8d illustrates the differential charge density diagrams of the Fe-N-C/Nb₄C₃T_x for OOH adsorption, featuring an adsorption energy of -3.476 eV. Upon integration of the Fe-N-C with the Nb₄C₃T_x, predominant active sites are localized at the Fe and N atoms from the Fe-N-C. Notably, there emerges a distinct contrast in the electron cloud distributions between the OOH and Fe-N-C as compared to that with the Nb₄C₃T_x. These phenomena ultimately facilitate the electron migration between the OOH and the Fe-N-C moieties in this research.

Fig. 9a affords the OER/ORR mechanistic diagram on the Fe-N-C/Nb₄C₃T_x under the alkaline conditions, revealing the interconnection between the OER and ORR. Fig. 9b shows the free energy ladder diagram of the investigated catalysts. Apparently, the Fe-N-C/Nb₄C₃T_x has the lowest energy barriers, particularly at the rate-limiting steps of the OH* for the ORR and the OOH* for the OER, outperforming those of isolated Fe-N-C and Nb₄C₃T_x counterparts (Table S7-8). Fig. 9c presents the respective diagram for the HER, the energy barrier is also the lowest for the Fe-N-C/Nb₄C₃T_x as opposed to the individual Fe-N-C and Nb₄C₃T_x (Table S7), particularly at the rate-limiting step of the H*.

Finally, the density of states (DOS) were compared for the Fe-N-C/Nb₄C₃T_x, Nb₄C₃T_x, and Fe-N-C (Fig. 9d). The results indicate that the incorporated Fe in the Fe-N-C and Nb in the Nb₄C₃T_x achieve sufficient covalent bonding, improving the structural stability and alleviating the polarization after formation of the O-functional group. As well, the introduced Fe-N-C also slightly elevates the Fermi level and enhances the electric conductivity. The synergistic effect of the Fe-N-C/Nb₄C₃T_x is expected as a trifunctional catalyst to enhance the electrochemical performance of Zn-air batteries.

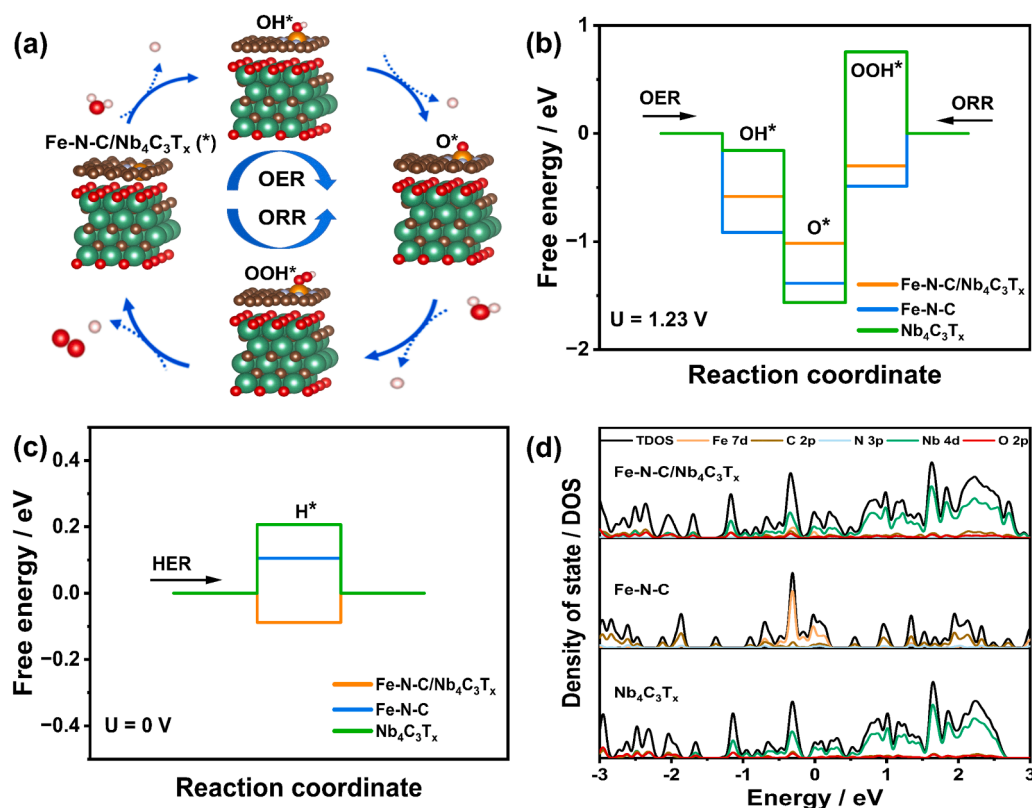


Fig. 9. (a) The ORR/ORR mechanistic diagram on the Fe-N-C/Nb₄C₃T_x catalyst sites. Free energy ladder diagram of the Nb₄C₃T_x, Fe-N-C, and Fe-N-C/Nb₄C₃T_x catalysts for the; (b) OER/ORR at U = 1.23 V, and (c) HER at U = 0 V. (d) DOS of the Nb₄C₃T_x, Fe-N-C, and Fe-N-C/Nb₄C₃T_x.

3.5. Application in Zn-air batteries

In light of the significant improvement in the ORR and OER activities, a home-made rechargeable battery was built by employing a freshly-polished Zn plate as the anode, the Fe-N-C/Nb₄C₃T_x (2:1) modified carbon paper as the cathode, and the cell-electrolyte containing 6.0 M KOH and 0.2 M zinc acetate (Fig. 10a). Inset in Fig. 10b presents the open-circuit potential of 1.51 V for the Fe-N-C/Nb₄C₃T_x (2:1)-based battery, which is greater than that of the Pt/C + RuO₂ control battery (1.43 V). Interestingly, the Fe-N-C/Nb₄C₃T_x (2:1) derived battery shows the substantially lower charging/discharging potential gap than its Pt/C+RuO₂ assembled counterpart (Fig. 10c), demonstrating its remarkable recharge capability [2,4,28]. As Fig. 10d shows, the Fe-N-C/Nb₄C₃T_x (2:1)-based battery exhibits a significantly higher peak power density of 136 mW cm⁻² than the Pt/C + RuO₂ counterpart (80 mW cm⁻²), coupled by surpassing the metal carbides, nitrides, and oxides-based batteries previously reported (Table 2) [2,4,19,21,28,39,60–62,70,71]. It certifies the outstanding discharging capabilities of the Fe-N-C/Nb₄C₃T_x-based battery.

The prolonged cycling stability of such battery was critically examined by increasing its working period (Fig. 10e). When the assembled Fe-N-C/Nb₄C₃T_x (2:1)-based battery is powered at 5 mA cm⁻² for 220 h (20 min/cycles, 660 cycles), the final voltage gap (0.85 V) is nearly equal to the initial one (0.87 V), while the Pt/C + RuO₂-based battery exhibits steep attenuation within 60 h [2,4,39]. These scenarios demonstrate the increased long-term endurance of the Fe-N-C/Nb₄C₃T_x-assembled battery and its future applicability. In addition, a red light-emitting diode (LED, 2.0 V) can be illuminated by connecting two Zn-air cells in series with the Fe-N-C/Nb₄C₃T_x (2:1) as the cathodic catalyst (Fig. 10a). Clearly, the as-fabricated electrocatalyst holds great potential in high-tech metal-air batteries.

Simultaneously, the stability of the Fe-N-C/Nb₄C₃T_x (2:1) was validated through the XRD (Fig. S4c) and SEM (Fig. S4d) analysis after the prolonged charge-discharge cycling test. In brief, the XRD diffraction patterns of the Fe-N-C/Nb₄C₃T_x (2:1) remain consistent before and after such measures, albeit with an increase in the peak intensities due to its partial oxidation. In parallel, noticeable holes are observed within the spherical nanosheets after the associated cycling test for the Fe-N-C/

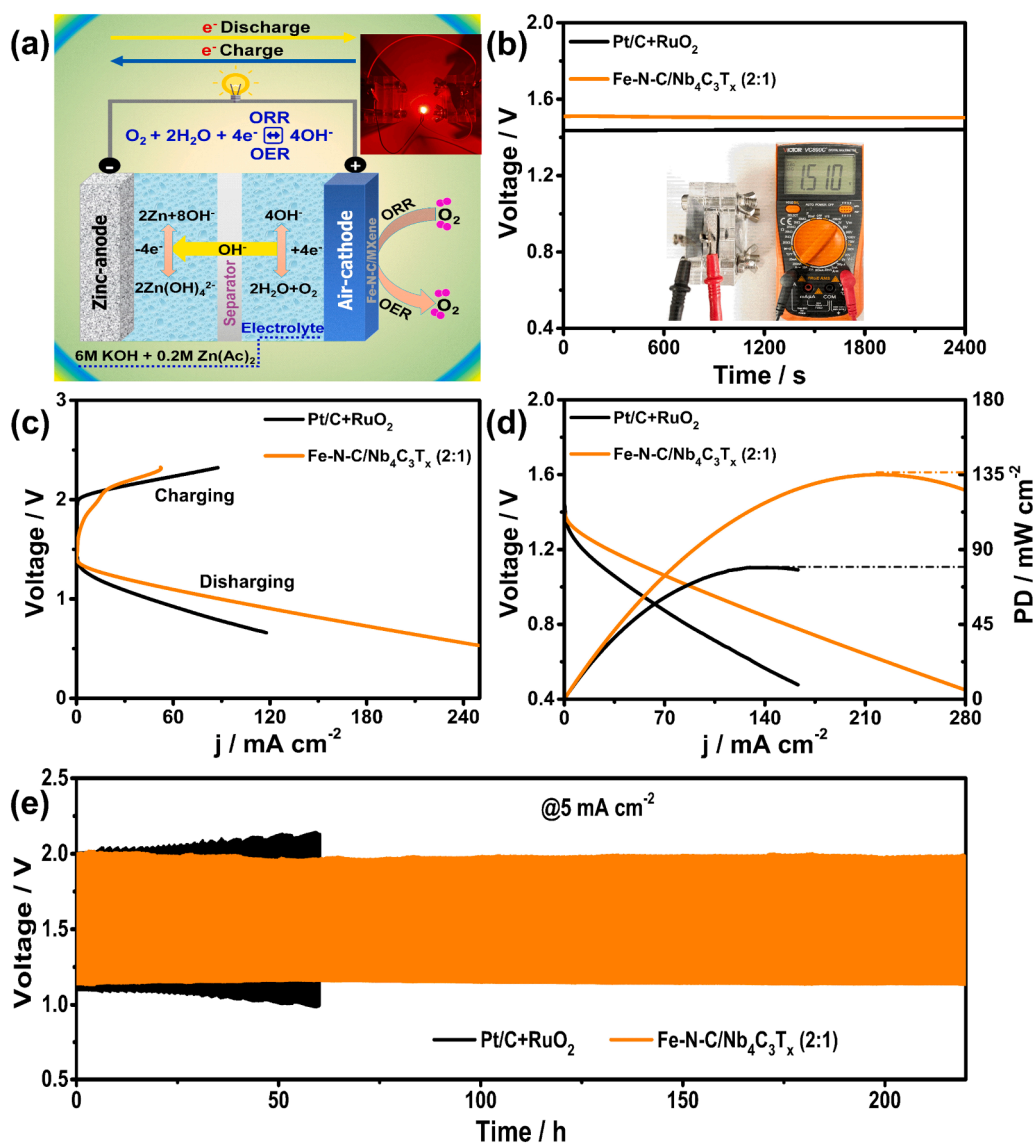


Fig. 10. (a) Schematic illustration of the assembly of the rechargeable liquid Zn-air battery; Inset shows the photograph of a red LED (2.0 V) powered by two batteries based on the Fe-N-C/Nb₄C₃T_x (2:1). (b) Open circuit voltages; Inset shows the photograph of the open circuit voltage for the Fe-N-C/Nb₄C₃T_x (2:1)-based battery. (c) Charge and discharge polarization curves. (d) Polarization curves and power density curves. (e) Long-term galvanostatic charge-discharge cycling curves of the Fe-N-C/Nb₄C₃T_x (2:1) and control Pt/C+RuO₂ based batteries at a current density of 5 mA cm⁻².

Nb₄C₃T_x (2:1). These holes are linked to the erosion caused by water or airflow. The surface holes enhance the contact between the oxygen-containing intermediates and the active sites of the Fe-N-C/Nb₄C₃T_x, thereby facilitating the electrocatalytic characteristics.

The outstanding electrocatalytic performances of the assembled Fe-N-C/Nb₄C₃T_x-based battery is mainly attributed to the distinct porous texture, suitable degree of graphitization, and synergistic impact of the Fe-N-C with the Nb₄C₃T_x, which favor strong mass and charge transport via the diffusion channels. First, the sheet-like Nb₄C₃T_x provides a 2D platform for uniform circulation of the Fe-N-C active sites with extra surface area that enables effective contact with the oxygen-containing species to accelerate the electrocatalysis [2,4]. Second, the high proportion of oxygen vacancies and enriched active sites play influential roles in rapid O₂ diffusion and charge transfer from the diffusion channels, resulting in the high electrical conductivity [2,53,59]. Last, the synergistic influences between the heteroatoms, transition metals, and carbon matrix would create the localized active sites, increase the stability, lower the kinetics and energy barriers, thus accelerating the trifunctional electrocatalytic activities in Zn-air batteries [28,39,71].

4. Conclusions

In summary, a class of the Fe-N-C/MXene derived trifunctional electrocatalysts were synthesized by electrochemical etching and wet-chemical treatment, followed by low-temperature pyrolysis. The optimal Fe-N-C/Nb₄C₃T_x exhibited higher catalytic performances for the ORR ($E_{1/2}$ = 0.911 V), OER (η_{10} = 1.52 V), and HER (η_{10} = 91 mV) vs. RHE in the alkaline electrolyte, outperforming previous metal carbides, nitrides, and oxides catalysts. Furthermore, the catalyst's practicality is demonstrated through its applications in the water splitting electrolyzer and rechargeable battery, only requiring 1.58 V at 10 mA cm⁻². Besides, the derived battery delivered a greater power density (136 mW cm⁻²), a lower charging/discharging potential gap (0.85 V) at 5 mA cm⁻², and superior stability even after the operation for 220 h. This research also integrated the DFT calculations to guide catalyst design, provides insightful information for developing high-quality multifunctional catalysts based on non-noble metals in high-tech energy-related devices.

CRediT authorship contribution statement

Mahmood ul Haq: Data curation, Formal analysis, Writing – original draft. **Dong-Hui Wu:** Data curation, Formal analysis. **Zeeshan Ajmal:** Data curation, Formal analysis. **Qi-Dong Ruan:** Data curation, Formal analysis. **Shahid Khan:** Investigation, Methodology. **Lu Zhang:** Investigation, Methodology. **Ai-Jun Wang:** Investigation, Methodology, Writing – review & editing. **Jiu-Ju Feng:** Investigation, Methodology, Writing – review & editing.

Declaration of Competing Interest

The authors declare that they have no known competing financial interests or personal relationships that could have appeared to influence the work reported in this paper.

Data availability

Data will be made available on request.

Acknowledgments

This work was financially supported by the National Natural Science Foundation of China (No. 21805245) and China Postdoctoral Start-up Research Grant (No. ZC304022921).

Appendix A. Supporting information

Supplementary data associated with this article can be found in the online version at doi:10.1016/j.apcatb.2023.123632.

References

- [1] L. Yan, Y. Xu, P. Chen, S. Zhang, H. Jiang, L. Yang, Y. Wang, L. Zhang, J. Shen, X. Zhao, L. Wang, A freestanding 3D heterostructure film stitched by MOF-derived carbon nanotube microsphere superstructure and reduced graphene oxide sheets: a superior multifunctional electrode for overall water splitting and Zn-air batteries, *Adv. Mater.* 32 (2020), 2003313, <https://doi.org/10.1002/adma.202003313>.
- [2] Z. Zeng, G. Fu, H.B. Yang, Y. Yan, J. Chen, Z. Yu, J. Gao, L.Y. Gan, B. Liu, P. Chen, Bifunctional N-CoSe₂/3D-MXene as highly efficient and durable cathode for rechargeable Zn-air battery, *ACS Mater. Lett.* 1 (2019) 432–439, <https://doi.org/10.1021/acsmaterialslett.9b00337>.
- [3] J. Pang, R.G. Mendes, A. Bachmatiuk, L. Zhao, H.Q. Ta, T. Gemming, H. Liu, Z. Liu, M.H. Rummeli, Applications of 2D MXenes in energy conversion and storage systems, *Chem. Soc. Rev.* 48 (2019) 72–133, <https://doi.org/10.1039/C8CS00324F>.
- [4] S. Han, Y. Chen, Y. Hao, Y. Xie, D. Xie, Y. Chen, Y. Xiong, Z. He, F. Hu, L. Li, J. Zhu, Multi-dimensional hierarchical CoS₂/MXene as trifunctional electrocatalysts for Zn-air batteries and overall water splitting, *Sci. China Mater.* 64 (2021) 1127–1138, <https://doi.org/10.1007/s40843-020-1524-5>.
- [5] Q. Qin, H. Jang, P. Li, B. Yuan, X. Liu, J. Cho, A tannic acid-derived N-, P-codoped carbon-supported iron-based nanocomposite as an advanced trifunctional electrocatalyst for the overall water splitting cells and Zinc-air batteries, *Adv. Energy Mater.* 9 (2019), 1803312, <https://doi.org/10.1002/aenm.201803312>.
- [6] Y. Li, R. Cao, L. Li, X. Tang, T. Chu, B. Huang, K. Yuan, Y. Chen, Simultaneously integrating single atomic cobalt sites and Co₉S₈ nanoparticles into hollow carbon nanotubes as trifunctional electrocatalysts for Zn-air batteries to drive water splitting, *Small* 16 (2020), 1906735, <https://doi.org/10.1002/sml.201906735>.
- [7] J. Li, Z. Meng, D.J. Brett, P.R. Shearing, N.T. Skipper, I.P. Parkin, S. Gadipelli, High-performance zinc-air batteries with scalable metal-organic frameworks and platinum carbon black bifunctional catalysts, *ACS Appl. Mater. Interf.* 12 (2020) 42696–42703, <https://doi.org/10.1021/acsaami.0c10151>.
- [8] S. Chen, L.L. Zhao, J.Z. Ma, Y.Q. Wang, L.M. Dai, J.T. Zhang, Edge-doping modulation of N, P-codoped porous carbon spheres for high-performance rechargeable Zn-air batteries, *Nano Energy* 60 (2019) 536–544, <https://doi.org/10.1016/j.nanoen.2019.03.084>.
- [9] P. Zhang, D. Bin, J.S. Wei, X.Q. Niu, X.B. Chen, Y.Y. Xia, H.M. Xiong, Efficient oxygen electrocatalyst for Zn-air batteries: carbon dots and Co₉S₈ nanoparticles in a N, S-codoped carbon matrix, *ACS Appl. Mater. Interf.* 11 (2019) 14085–14094, <https://doi.org/10.1021/acsaami.8b22557>.
- [10] Q. Liang, H. Jin, Z. Wang, Y. Xiong, S. Yuan, X. Zeng, D. He, S. Mu, Metal-organic frameworks derived reverse-encapsulation Co-NC@Mo₂C complex for efficient overall water splitting, *Nano Energy* 57 (2019) 746–752, <https://doi.org/10.1016/j.nanoen.2018.12.060>.
- [11] T. Li, Y. Lu, S. Zhao, Z.D. Gao, Y.Y. Song, Co₃O₄-doped Co/CoFe nanoparticles encapsulated in carbon shells as bifunctional electrocatalysts for rechargeable Zn-air batteries, *J. Mater. Chem. A* 6 (2018) 3730–3737, <https://doi.org/10.1039/C7TA11171A>.
- [12] W. Niu, S. Pakhira, K. Marcus, Z. Li, J.L. Mendoza-Cortes, Y. Yang, Apically dominant mechanism for improving catalytic activities of N-doped carbon nanotube arrays in rechargeable Zinc-air battery, *Adv. Energy Mater.* 8 (2018), 1800480, <https://doi.org/10.1002/aenm.201800480>.
- [13] L. Jiao, G. Wan, R. Zhang, H. Zhou, S.H. Yu, H.L. Jiang, From metal-organic frameworks to single-atom Fe implanted N-doped porous carbons: efficient oxygen reduction in both alkaline and acidic media, *Angew. Chem., Int. Ed.* 57 (2018) 8525–8529, <https://doi.org/10.1002/ange.201803262>.
- [14] Y.S. Wei, M. Zhang, R. Zou, Q. Xu, Metal-organic framework-based catalysts with single metal sites, *Chem. Rev.* 120 (2020) 12089–12174, <https://doi.org/10.1021/acs.chemrev.9b00757>.
- [15] M. Xiao, J. Zhu, L. Ma, Z. Jin, J. Ge, X. Deng, Y. Hou, Q. He, J. Li, Q. Jia, S. Mukerjee, Microporous framework induced synthesis of single-atom dispersed Fe-NC acidic ORR catalyst and its in situ reduced Fe-N₄ active site identification revealed by X-ray absorption spectroscopy, *ACS Catal.* 8 (2018) 2824–2832, <https://doi.org/10.1021/acscatal.8b00138>.
- [16] G. Zou, H. Hou, P. Ge, Z. Huang, G. Zhao, D. Yin, X. Ji, Metal-organic framework derived materials for sodium energy storage, *Small* 14 (2017), 1702648, <https://doi.org/10.1002/sml.201702648>.
- [17] H. Zhang, X. Liu, Y. Wu, C. Guan, A.K. Cheetham, J. Wang, MOF-derived nanohybrids for electrocatalysis and energy storage: current status and perspectives, *Chem. Commun.* 54 (2018) 5268–5288, <https://doi.org/10.1039/C8CC00789F>.
- [18] D. Villers, X. Jacques-Bedard, J.P. Dodelet, Fe-based catalysts for oxygen reduction in PEM fuel cells: pretreatment of the carbon support, *J. Electrochem. Soc.* 151 (2004) A1507–A1515, <https://doi.org/10.1149/1.1781611>.
- [19] Y. Guo, P. Yuan, J. Zhang, H. Xia, F. Cheng, M. Zhou, J. Li, Y. Qiao, S. Mu, Q. Xu, Co₂P-CoN double active centers confined in N-doped carbon nanotube: heterostructural engineering for trifunctional catalysis toward HER, ORR, OER, and Zn-air batteries driven water splitting, *Adv. Funct. Mater.* 28 (2018), 1805641, <https://doi.org/10.1002/adfm.201805641>.

- [20] C. Wang, H. Zhao, J. Wang, Z. Zhao, M. Cheng, X. Duan, Q. Zhang, J. Wang, J. Wang, Atomic Fe hetero-layered coordination between g-C₃N₄ and graphene nanomeshes enhances the ORR electrocatalytic performance of Zinc-air batteries, *J. Mater. Chem. A* 7 (2019) 1451–1458, <https://doi.org/10.1039/C8TA09722D>.
- [21] Q. Wang, Y. Lei, Z. Chen, N. Wu, Y. Wang, B. Wang, Y. Wang, Fe/Fe₃C@C nanoparticles encapsulated in N-doped graphene-CNTs framework as an efficient bifunctional oxygen electrocatalyst for robust rechargeable Zn-air batteries, *J. Mater. Chem. A* 6 (2018) 516–526, <https://doi.org/10.1039/C7TA08423D>.
- [22] W. Niu, Y. Yang, Amorphous MOF introduced N-doped graphene: an efficient and versatile electrocatalyst for Zinc-air battery and water splitting, *ACS Appl. Energy Mater.* 1 (2018) 2440–2445, <https://doi.org/10.1021/acs.aem.8b00594>.
- [23] X. Zhang, J. Luo, H.F. Lin, P. Tang, J.R. Morante, J. Arbiol, K. Wan, B.W. Mao, L. M. Liu, J. Fransaer, Tailor-made metal-nitrogen-carbon bifunctional electrocatalysts for rechargeable Zn-air batteries via controllable MOF units, *Energy Storage Mater.* 17 (2019) 46–61, <https://doi.org/10.1016/j.ensm.2018.11.034>.
- [24] M. Naguib, M. Kurtoglu, V. Presser, J. Lu, J. Niu, M. Heon, L. Hultman, Y. Gogotsi, M.W. Barsoum, Two-dimensional nanocrystals produced by exfoliation of Ti₃AlC₂, *Adv. Mater.* 23 (2011) 4248–4253, <https://doi.org/10.1002/adma.201102306>.
- [25] W. Zaman, R.A. Matsumoto, M.W. Thompson, Y.H. Liu, Y. Bootwala, M.B. Dixit, S. Nemsak, E. Crumlin, M.C. Hatzell, P.T. Cummings, K.B. Hatzell, In situ investigation of water on MXene interfaces, *Proc. Natl. Acad. Sci. U. S. A.* 118 (2021), e2108325118, <https://doi.org/10.1073/pnas.2108325118>.
- [26] Z. Wang, K. Yu, Y. Feng, R. Qi, J. Ren, Z. Zhu, VO₂(p)-V₂C(MXene) grid structure as a lithium polysulfide catalytic host for high-performance Li-S battery, *ACS Appl. Mater. Interf.* 11 (2019) 44282–44292, <https://doi.org/10.1021/acsami.9b15586>.
- [27] G. Li, N. Li, S. Peng, B. He, J. Wang, Y. Du, W. Zhang, K. Han, F. Dang, Highly efficient Nb₂C MXene cathode catalyst with uniform O-terminated surface for lithium-oxygen batteries, *Adv. Energy Mater.* 11 (2020), 2002721, <https://doi.org/10.1002/aenm.202002721>.
- [28] C. Zhang, H. Dong, B. Chen, T. Jin, J. Nie, G. Ma, 3D MXene anchored carbon nanotube as bifunctional and durable oxygen catalysts for Zn-air batteries, *Carbon* 185 (2021) 17–26, <https://doi.org/10.1016/j.carbon.2021.09.004>.
- [29] D. Kan, D. Wang, Y. Cheng, R. Lian, B. Sun, K. Chen, W. Huo, Y. Wang, G. Chen, Y. Wei, Designing of efficient bifunctional ORR/OER Pt single-atom catalysts based on O-terminated MXenes by first-principles calculations, *ACS Appl. Mater. Interf.* 13 (2021) 52508–52518, <https://doi.org/10.1021/acsami.1c12893>.
- [30] C.F. Du, Q.T. Song, Q.H. Liang, X.Y. Zhao, J.J. Wang, R.C. Zhi, Y.X. Wang, H. Yu, The passive effect of MXene on electrocatalysis: a case of Ti₃C₂T_x/CoNi-MOF nanosheets for oxygen evolution reaction, *ChemNanoMat* 7 (2021) 539–544, <https://doi.org/10.1002/cnma.202100061>.
- [31] W.T. Wang, N. Batool, T.H. Zhang, J. Liu, X.F. Han, J.H. Tian, R. Yang, When MOFs meet MXenes: superior ORR performance in both alkaline and acidic solutions, *J. Mater. Chem. A* 9 (2021) 3952–3960, <https://doi.org/10.1039/D0TA10811A>.
- [32] W. Sun, S.A. Shah, Y. Chen, Z. Tan, H. Gao, T. Habib, M. Radovic, M.J. Green, Electrochemical etching of Ti₂AlC to Ti₂CT_x (MXene) in low-concentration hydrochloric acid solution, *J. Mater. Chem. A* 5 (2017) 21663–21668, <https://doi.org/10.1039/C7TA05574A>.
- [33] G. Kresse, D. Joubert, From ultrasoft pseudopotentials to the projector augmented-wave method, *Phys. Rev. B* 59 (1999) 1758–1770, <https://doi.org/10.1103/PhysRevB.59.1758>.
- [34] J.P. Perdew, K. Burke, M. Ernzerhof, Generalized gradient approximation made simple, *Phys. Rev. Lett.* 77 (1996) 3865–3868, <https://doi.org/10.1103/PhysRevLett.77.3865>.
- [35] L. Yu, L. Hu, B. Anasori, Y.T. Liu, Q. Zhu, P. Zhang, Y. Gogotsi, B. Xu, MXene-bonded activated carbon as a flexible electrode for high-performance supercapacitors, *ACS Energy Lett.* 3 (2018) 1597–1603, <https://doi.org/10.1021/acsenergylett.8b00718>.
- [36] J. Yan, T. Wei, B. Shao, F. Ma, Z. Fan, M. Zhang, C. Zheng, Y. Shang, W. Qian, F. Wei, Electrochemical properties of graphene nanosheet/carbon black composites as electrodes for supercapacitors, *Carbon* 48 (2010) 1731–1737, <https://doi.org/10.1016/j.carbon.2010.01.014>.
- [37] M.R. Lukatskaya, J. Halim, B. Dyatkin, M. Naguib, Y.S. Buranova, M.W. Barsoum, Y. Gogotsi, Room-temperature carbide-derived carbon synthesis by electrochemical etching of MAX phases, *Angew. Chem. Int. Ed.* 53 (2014) 4877–4880, <https://doi.org/10.1002/ange.201402513>.
- [38] S.J. Bao, C.M. Li, J.F. Zang, X.Q. Cui, Y. Qiao, J. Guo, New nanostructured TiO₂ for direct electrochemistry and glucose sensor applications, *Adv. Funct. Mater.* 18 (2008) 591–599, <https://doi.org/10.1002/adfm.200700728>.
- [39] H. Zong, W. Liu, M. Li, S. Gong, K. Yu, Z. Zhu, Oxygen-terminated Nb₂CO₂ MXene with interfacial self-assembled COF as a bifunctional catalyst for durable zinc-air batteries, *ACS Appl. Mater. Interf.* 14 (2022) 10738–10746, <https://doi.org/10.1021/acsami.1c25264>.
- [40] H. Tian, A. Song, P. Zhang, K. Sun, J. Wang, B. Sun, Q. Fan, G. Shao, C. Chen, H. Liu, Y. Li, High durability of Fe-N-C single-atom catalysts with carbon vacancies toward the oxygen reduction reaction in alkaline media, *Adv. Mater.* 35 (2023), 2210714, <https://doi.org/10.1002/adma.202210714>.
- [41] H. Meng, X. Chen, T. Gong, H. Liu, Y. Liu, H. Li, Y. Zhang, N. P, S/Fe-codoped carbon derived from feculae bombycis as an efficient electrocatalyst for oxygen reduction reaction, *ChemCatChem* 11 (2019) 6015–6021, <https://doi.org/10.1002/cctc.201900604>.
- [42] L. Zheng, J. Wang, Y. Zhou, Improving the high-temperature oxidation resistance of Nb₄AlC₃ by silicon pack cementation, *J. Am. Ceram. Soc.* 97 (2014) 552–561, <https://doi.org/10.1111/jace.12667>.
- [43] P.A. Rasheed, R.P. Pandey, T. Gomez, K.A. Jabbar, K. Prenger, M. Naguib, B. Aïssa, K.A. Mahmoud, Nb-based MXenes for efficient electrochemical sensing of small biomolecules in the anodic potential, *Electrochem. Commun.* 119 (2020), 106811, <https://doi.org/10.1016/j.elecom.2020.106811>.
- [44] C. Hu, F. Li, J. Zhang, J. Wang, J. Wang, Y. Zhou, Nb₄AlC₃: a new compound belonging to the MAX phases, *Scr. Mater.* 57 (2007) 893–896, <https://doi.org/10.1016/j.scriptamat.2007.07.038>.
- [45] M. Alhabeb, K. Maleski, B. Anasori, P. Lelyukh, L. Clark, S. Sin, Y. Gogotsi, Guidelines for synthesis and processing of two-dimensional titanium carbide (Ti₃C₂T_x MXene), *Chem. Mater.* 29 (2017) 7633–7644, <https://doi.org/10.1021/acs.chemmater.7b02847>.
- [46] Z. Li, Z. Zhuang, F. Lv, H. Zhu, L. Zhou, M. Luo, J. Zhu, Z. Lang, S. Feng, W. Chen, L. Mai, The marriage of the FeN₄ moiety and MXene boosts oxygen reduction catalysis: Fe3d electron delocalization matters, *Adv. Mater.* 30 (2018), 1803220, <https://doi.org/10.1002/adma.201803220>.
- [47] L. Cao, X. Zhou, Z. Li, K. Su, B. Cheng, Nitrogen and fluorine hybridization state tuning in hierarchical honeycomb-like carbon nanofibers for optimized electrocatalytic ORR in alkaline and acidic electrolytes, *J. Pow. Sour.* 413 (2019) 376–383, <https://doi.org/10.1016/j.jpowsour.2018.12.076>.
- [48] X. Chen, N. Wang, K. Shen, Y. Xie, Y. Tan, Y. Li, MOF-derived isolated Fe atoms implanted in N-doped 3D hierarchical carbon as an efficient ORR electrocatalyst in both alkaline and acidic media, *ACS Appl. Mater. Interf.* 11 (2019) 25976–25985, <https://doi.org/10.1021/acsami.9b07436>.
- [49] S. Li, C. Cheng, X. Zhao, J. Schmidt, A. Thomas, Active salt/silica-templated 2D mesoporous FeCo-N_x-carbon as bifunctional oxygen electrodes for Zinc-air batteries, *Angew. Chem. Int. Ed.* 57 (2018) 1856–1862, <https://doi.org/10.1002/anie.201710852>.
- [50] M. Lubke, J. Shin, P. Marchand, D. Brett, P. Shearing, Z. Liub, J.A. Darr, Highly pseudocapacitive Nb-doped TiO₂ high power anodes for lithium-ion batteries, *J. Mater. Chem. A* 3 (2015) 22908–22914, <https://doi.org/10.1039/C5TA07554H>.
- [51] A. Gupta, M. Mittal, M.K. Singh, S.L. Suib, O.P. Pandey, Low temperature synthesis of NbC/C nano-composites as visible light photoactive catalyst, *Sci. Rep.* 8 (2018), 13597, <https://doi.org/10.1038/s41598-018-31989-z>.
- [52] G.L. Wen, H.J. Niu, A.J. Wang, Z.Z. Yin, Q.L. Zhang, J.J. Feng, Graphene wrapped Fe₂C₃ nanoparticles supported on N-doped graphene nanosheets for efficient and highly methanol-tolerant oxygen reduction reaction, *J. Colloid Interf. Sci.* 556 (2019) 352–359, <https://doi.org/10.1016/j.jcis.2019.08.064>.
- [53] H.J. Niu, S.Y. Lin, Y.P. Chen, J.J. Feng, Q.L. Zhang, A.J. Wang, Hydrogel derived FeCo/FeCoP embedded in N, P-codoped 3D porous carbon framework as a highly efficient electrocatalyst for oxygen reduction reaction, *Appl. Surf. Sci.* 536 (2021), 147950, <https://doi.org/10.1016/j.apsusc.2020.147950>.
- [54] X. Dong, H. Jin, R. Wang, J. Zhang, X. Feng, C. Yan, S. Chen, S. Wang, J. Wang, J. Lu, High volumetric capacitance, ultralong life supercapacitors enabled by waxberry-derived hierarchical porous carbon materials, *Adv. Energy Mater.* 8 (2018), 1702695, <https://doi.org/10.1002/aenm.201702695>.
- [55] C.C. Yang, S.F. Zai, Y.T. Zhou, L. Du, Q. Jiang, Fe₃C-Co nanoparticles encapsulated in a hierarchical structure of N-doped carbon as a multifunctional electrocatalyst for ORR, OER, and HER, *Adv. Funct. Mater.* 29 (2019), 1901949, <https://doi.org/10.1002/adfm.201901949>.
- [56] A. Zhu, L. Qiao, P. Tan, Y. Ma, W. Zeng, R. Dong, C. Ma, J. Pan, Iron-nitrogen carbon species for oxygen electro-reduction and Zn-air battery: surface engineering and experimental probe into active sites, *254, Appl. Catal., B* 254 (2019) 601–611, <https://doi.org/10.1016/j.apcatb.2019.05.037>.
- [57] Q. Xue, Z. Pei, Y. Huang, M. Zhu, Z. Tang, H. Li, Y. Huang, N. Li, H. Zhang, C. Zhi, Mn₃O₄ nanoparticles on layer-structured Ti₃C₂ MXene towards the oxygen reduction reaction and Zinc-air batteries, *J. Mater. Chem. A* 5 (2017) 20818–20823, <https://doi.org/10.1039/C7TA04532H>.
- [58] Y. Zhang, H. Jiang, Y. Lin, H. Liu, Q. He, C. Wu, T. Duan, L. Song, In situ growth of cobalt nanoparticles encapsulated nitrogen-doped carbon nanotubes among Ti₃C₂T_x (MXene) matrix for oxygen reduction and evolution, *Adv. Mater. Interf.* 5 (2018), 1800392, <https://doi.org/10.1002/admi.201800392>.
- [59] P. Zhang, R. Wang, T. Xiao, Z. Chang, Z. Fang, Z. Zhu, C. Xu, L. Wang, J. Cheng, The high-performance bifunctional catalyst Pd/Ti₃C₂T_x-carbon nanotube for oxygen reduction reaction and hydrogen evolution reaction in alkaline medium, *Energy Tech.* 8 (2020), 2000306, <https://doi.org/10.1002/ente.202000306>.
- [60] H. Lei, S. Tan, L. Ma, Y. Liu, Y. Liang, M.S. Javed, Z. Wang, Z. Zhu, W. Mai, Strongly coupled NiCo₂O₄ nanocrystal/MXene hybrid through in situ Ni/Co-F bonds for efficient wearable Zn-air batteries, *ACS Appl. Mater. Interf.* 12 (2020) 44639–44647, <https://doi.org/10.1021/acsami.0c11185>.
- [61] H. Zou, B. He, P. Kuang, J. Yu, K. Fan, Metal-organic framework derived nickel-cobalt sulfide on ultrathin mxene nanosheets for electrocatalytic oxygen evolution, *ACS Appl. Mater. Interf.* 10 (2018) 22311–22319, <https://doi.org/10.1021/acsami.8b06272>.
- [62] Z. Wu, H. Wang, P. Xiong, G. Li, T. Qiu, W.B. Gong, F. Zhao, C. Li, Q. Li, G. Wang, F. Geng, Molecularly thin nitride sheets stabilized by titanium carbide as efficient bifunctional electrocatalysts for fiber-shaped rechargeable Zinc-air batteries, *Nano Lett.* 20 (2020) 2892–2898, <https://doi.org/10.1021/acs.nanolett.0c00717>.
- [63] N. Sekar, R.P. Ramasamy, Electrochemical impedance spectroscopy for microbial fuel cell characterization, *J. Microb. Biochem. Technol.* 6 (2013) 1–4, <https://doi.org/10.4172/1948-5948.S6-004>.
- [64] L. Xiu, Z. Wang, M. Yu, X. Wu, J. Qiu, Aggregation-resistant 3D MXene-based architecture as efficient bifunctional electrocatalyst for overall water splitting, *ACS Nano* 12 (2018) 8017–8028, <https://doi.org/10.1021/acs.nano.8b02849>.
- [65] C.F. Du, K.N. Dinh, Q. Liang, Y. Zheng, Y. Luo, J. Zhang, Q. Yan, Self-assemble and in situ formation of Ni_{1-x}Fe_xPS₃ nanomosaic-decorated MXene hybrids for overall water splitting, *Adv. Energy Mater.* 8 (2018), 1801127, <https://doi.org/10.1002/aenm.201801127>.

- [66] S.A. Zahra, S. Rizwan, MWCNT-modified MXene as cost-effective efficient bifunctional catalyst for overall water splitting, *RSC Adv.* 12 (2022) 8405–8413, <https://doi.org/10.1039/D2RA00868H>.
- [67] S.Y. Pang, Y.T. Wong, S. Yuan, Y. Liu, M.K. Tsang, Z. Yang, H. Huang, W.T. Wong, J. Hao, Universal strategy for HF-free facile and rapid synthesis of two-dimensional MXenes as multifunctional energy materials, *J. Am. Chem. Soc.* 141 (2019) 9610–9616, <https://doi.org/10.1021/jacs.9b02578>.
- [68] H. Zong, K. Yu, Z. Zhu, Heterostructure nanohybrids of Ni-doped MoSe₂ coupled with Ti₂NT_x toward efficient overall water splitting, *Electrochim. Acta* 353 (2020), 136598, <https://doi.org/10.1016/j.electacta.2020.136598>.
- [69] X.D. Zhu, Y. Xie, Y.T. Liu, Exploring the synergy of 2D MXene-supported black phosphorus quantum dots in hydrogen and oxygen evolution reactions, *J. Mater. Chem. A* 6 (2018) 21255–21260, <https://doi.org/10.1039/C8TA08374F>.
- [70] J. Chen, C. Fan, X. Hu, C. Wang, Z. Huang, G. Fu, J.M. Lee, Y. Tang, Hierarchically porous Co/Co_xM_y (M= P, N) as an efficient mott-schottky electrocatalyst for oxygen evolution in rechargeable Zn-air batteries, *Small* 15 (2019), 1901518, <https://doi.org/10.1002/sml.201901518>.
- [71] W. Cheng, P. Yuan, Z. Lv, Y. Guo, Y. Qiao, X. Xue, X. Liu, W. Bai, Q. Xu, J. Zhang, Boosting defective carbon by anchoring well-defined atomically dispersed metal-N₄ sites for ORR, OER, and Zn-air batteries, *Appl. Catal. B* 260 (2020), 118198, <https://doi.org/10.1016/j.apcatb.2019.118198>.